Relating Multi-Scale Plume Detection and Area Estimates of Methane Emissions: A Theoretical and Empirical Analysis

Sudhanshu Pandey,*,† John Worden,† Daniel H. Cusworth,‡ Daniel J. Varon,¶ Matthew D. Thill,† Daniel J. Jacob,¶ and Kevin W. Bowman†

†*Jet Propulsion Laboratory, California Institute of Technology, Pasadena, CA, 91109, USA*

‡*Carbon Mapper, Inc., Pasadena, CA, 91105, USA*

¶*School of Engineering and Applied Sciences, Harvard University, Cambridge, MA, 02138, USA*

E-mail: sudhanshu.pandey@jpl.nasa.gov

Abstract

Surface emissions of atmospheric trace gases are inferred using two main methodologies: plume detection and area-scale estimation. Integrating these methods can enhance emission monitoring but is challenging due to irregular sampling, varying detection sensitivities, and differing spatial pixel sizes of plume-detecting instruments. We present a theoretical framework to relate plume and area emission estimates in dense point-source emission fields. Our analysis shows that the spatial pixel size of plume-detecting instruments affects the distribution of emission rates. Empirical tests in the Permian Basin's oil and gas emissions reveal a robust linear relationship between the sums of gridded plume emission rates and area estimates. After accounting for

variations in plume detectors' sampling, TROPOMI inversion area estimates strongly correlate with weekly plume sums ($R^2 > 0.94, P < 0.005$). We assess the feasibility of using plume data to inform area estimates within a Bayesian assimilation framework, finding that plume assimilation improves the constant EDF inventory, bringing it into agreement with independent TROPOMI emission estimates. Our analysis demonstrates that, with adequate sampling under favorable observation conditions, plume datasets from aircraft, satellites, and in situ instruments can effectively evaluate and inform area emission estimates in the oil and gas sector.

Synopsis: We developed and validated a framework that links methane plumes to area emission estimates. We demonstrate how integrating plume data can improve regional methane emission estimates in dense point-source fields, such as the Permian Basin.

Keywords: oil, gas, inversions, fluxes, satellite, point-sources, Permian.

1 Introduction

Understanding methane emissions is crucial for developing climate change mitigation strategies and accurately predicting future climate. New observational techniques for detecting methane plumes from point sources have significantly advanced our understanding of methane emissions[1–12]. Reducing methane emissions—especially from large point sources (often called super-emitters), which can constitute a significant fraction of total emissions—is now central to climate change mitigation efforts[13–15]. Plumes are detected over a wide range of spatial scales (1 m to 10 km) but are limited to temporal snapshots ($<$ 1 hour) of the emissions from a single point source or a cluster of point sources. An area-scale observing system provides area-averaged estimates of emissions by aggregating emissions at spatial ($>$ 10 km) and temporal (>weekly) grid cells. Area estimates trade spatial resolution for improved accuracy in quantifying the total magnitude of emissions. In this paper, we present a theory that relates the sum of plume detections to area emission estimates over a region of dense point source emissions. We empirically test our theory using oil and gas sector emissions data from the Permian Basin. In turn, we demonstrate novel applications of plume data as tools for evaluating and informing area estimates in dense emission fields.

Area estimates of emissions are derived from bottom-up approaches[16,17] and top-down flux inversions[18–24]. Bottom-up inventories quantify emissions by combining emission factors (e.g., emission per wellhead) with activity data (e.g., number of wellheads). However, emission factors vary across operating conditions, leading to substantial inaccuracies in the emission estimates. Top-down approaches quantify emissions by comparing atmospheric chemical

transport model (CTM) simulations to observed atmospheric concentration gradients resulting from those emissions. The diffusive and chaotic nature of atmospheric transport, along with limited observation coverage and the computational cost of CTM simulations, limit the spatial resolution of top-down area estimates[25–28].

Plume detectors exploit sharp enhancements in a concentration field generated by a single point source or cluster of point sources. In situ plume-detecting instruments can be mounted on automobiles, aircraft, or the ground. Column-observing plume instruments are typically deployed onboard aircraft or satellites. These remote sensing instruments can be either active (e.g., LIDAR instruments;[29]) or passive (e.g., GHGSat, Sentinel-2, PRISMA, Carbon Mapper, MethaneSAT;[30–33]). Plume detections are used in Leak Detection and Repair (LDAR) techniques, focusing on fixing anomalous methane emitters to mitigate emissions. Observed plumes can account for a large fraction of the emission *rate* [kg hr^{-1}] in certain sectors, providing an advantage for targeted mitigation efforts[29,34,35].

A few studies have attempted to generate regional and national inventories that account for the large point source emissions absent in traditional bottom-up inventories[8,36–38]. These studies extrapolate plume detections from measured facilities, assuming some degree of temporal persistence in the emissions, and account for emissions below the detection limit of the instruments using bottom-up emission factors information[36]. Other studies have used plume detections to improve the prior emissions in the flux inversion estimates[39]. The distribution of plume emission rates also sheds light on emission mechanisms, highlighting opportunities for effective mitigation by addressing the contributions of large emitters to total emissions[29,34].

Because area estimate methods quantify the total emissions from one or multiple sectors together, they are directly related to regional total emissions. However, the relationship of plume detections to regional total emissions is complex for several reasons. First, the spatial resolution (or ground pixel size) varies by orders of magnitude among plume-detecting instruments: less than 20 m for hand-held Optical Gas Imaging (OGI) cameras as well as ground

and aerial in situ instruments[5,6,40–42], $1 - 150$ m for aerial imaging instruments[3,31,34,43,44], and 4 — 400 m for satellite imaging instruments[7,32,33,45,45–51]. The TROPOspheric Monitoring Instrument (TROPOMI), originally designed for providing top-down constraint in flux inversions, also observes methane plumes but at a pixel size of roughly 7 km[7,47,48,50,52–54]. Second, detection sensitivity varies significantly among plume instruments. For instance, Sentinel-2, a multi-band instrument with a 20-m pixel utilizing only spectral bands from the observation day, can detect point sources emitting over 1 t hr^{-1}[33]. GHGSat, with a similar spatial pixel, can detect plumes with emission rates below 100 kg hr^{-1} under favorable observation conditions[29,55,56]. Third, plumes only observe a fraction of the total emission *rate* [kg hr^{-1}] of a region for sectors. This emission rate fraction can be quite large depending on the instrument and sector. However, the detected mass enhancement in plumes represents only a tiny fraction of the total emitted *mass* [kg]. For instance, an aircraft campaign might sample the emissions field of a region for tens of hours over a year, observing only a very small mass fraction of the monthly or annual emissions. Plumes may represent a significant mass fraction of emissions if they originate from persistent sources. However, this assumption is not always valid[10,57]. Fourth, intermittent point source emissions can bias temporal mean estimates of emissions. Both in situ and passive total column imaging instruments tend to observe methane concentrations in the late morning or afternoon to detect point source or facility emissions. In situ instruments prefer a well-developed planetary boundary layer and passive imaging instruments prefer strong solar backscatter light. The diurnal cycle of oil and gas emissions can be pronounced at these times due to daytime maintenance operations[57,58]. Consequently, emission inferences based solely on afternoon data can be a biased estimate of the temporal mean of emissions.

We present a theory (Section 2) that relates plume detections and area estimates in dense point source emission fields. We derive a statistical relation between plume sums and area estimates, taking into account instrument detection sensitivity, sampling, and the periodicity of emissions. In Section 3, we describe the oil and gas emission datasets from the Permian

Basin used in this study. In Section 4, we test the statistical relationship between plume sums and area estimates using the Permian Basin data. In Section 5, we present approaches to evaluate and refine area emission estimates using plume sums. Finally, we discuss our findings in Section 6 and provide a summary in Section 7.

2 Theory

2.1 Definitions

Here we define and distinguish point sources, plume detection, and area emission estimates.

- **Point source**: A source of emission with a small spatial extent, less than a few meters, much smaller than or comparable to the spatial pixel size of any plume-observing instrument. Point sources can be infrastructure components that emit plumes of highly concentrated trace gas. The emission rate of a point source has the unit kg hr^{-1}.

- **Plume detection**: The detection of emissions from a single point source or a cluster of point sources, observed as a group of concentration-enhanced pixels by an imaging instrument. In situ instruments also detect plumes as a sharp enhancement in concentrations downwind of one or more point sources. The emission rate of a plume is given in the unit of kg hr^{-1}.

- **Area estimates**: Estimates of total emissions over a large spatial ($>$ 10 km) and temporal ($>$ week) interval for a sector or sum of sectors. Area estimates are derived using top-down flux inversions or bottom-up approaches. An area estimate of emissions has the unit kg hr^{-1} m^{-2}.

Emissions from point sources in a dense emission field, such as an oil and gas basin, can be observed both as area estimates and plume detections, but these observations have different spatial specificity, and they measure different proportions of total emissions. In the

literature, methane plume detections and point sources are sometimes used interchangeably, assuming a plume originates from a single point source. For our analysis, we emphasize distinguishing between a point source and a plume detection because a plume can contain emissions from multiple point sources[39,50].

A single plume detection entry in a dataset typically includes at least three values: (1) the plume's source location (latitude and longitude), (2) the time of detection, and (3) the emission rate with uncertainty estimates. Some plume datasets also provide wind speed data used for emission rate quantification, as wind is generally considered the main source of error in these calculations[59]. Area estimate datasets are typically provided in a gridded format where each grid cell represents the mean emission rate over specific spatial and temporal intervals. Some but not all area estimates include uncertainty estimates or even a full error covariance matrix[60,61]. However, calculating the full posterior error covariance becomes computationally expensive or even impractical when optimizing large state vectors in top-down approaches, which is often done using variational inversion methods[22,62]. The emission values may represent total emissions from a grid cell (typically from top-down inversions) or sector-specific emissions (typically from bottom-up inventories like EDGAR and EPA)[16,63]. Top-down flux inversions sometimes offer sectoral partitioning but still rely heavily on bottom-up information for sector attribution[24].

2.2 Conceptual Illustrations

Here, we conceptualize how the spatial pixel size of plume detectors can affect the number of possible plume detections and their emission rates when observing a dense point source emission field.

2.2.1 Impact of Instrument Pixel Size on Plume Detection

Consider an observing system monitoring a dense point source emission field within a grid cell c of size $l_c \times l_c$ [m^2]. The observing system uses a concentration imaging instrument i

with a spatial pixel of size $l_i \times l_i$ [m^2]. Then, the observed concentration field is a discrete representation of the underlying emission field, with resolution determined by the instrument's pixel size. Suppose the imaging instrument detects a plume by identifying a group of enhanced pixels forming a Gaussian plume shape. An enhanced pixel can be roughly defined as one where the concentration value exceeds the background by at least $2\sigma_i$, where σ_i is the instrument's pixel concentration precision. Let δ_i^2 [m^2] denote the area required to confidently detect a Gaussian-shaped plume. We define the square root of this area, δ_i [m], as the *emission spatial specificity*. δ_i quantifies the instrument's ability to differentiate emissions from distinct point sources.

To maintain clarity and simplicity in our conceptual exercises (Figures 1 and 2), we assume that δ_i is linearly dependent on l_i for instruments with similar concentration precision. This relationship assumes that the number of pixels required to detect a plume remains consistent across different scales. However, δ_i is also influenced by factors such as instrument concentration precision, which depends on its signal-to-noise ratio (SNR), wind speed, surface albedo, and the spatial distribution of point sources. Therefore, estimating δ_i for a specific instrument can be challenging. Our goal here is not to provide an exact estimate of δ_i but to highlight its impact on plume detection.

Figure 1 displays a snapshot of the column-averaged concentration field of a trace gas from a Weather Research and Forecasting model coupled with Chemistry (WRF-Chem) CTM simulation at 1×1 km^2 resolution with ten-point emission sources. Using this figure, we conceptually examine two physical effects on the number of plume detections (N): (1) reduction of N due to clustering of plumes from distinct point sources as l_i increases, and (2) reduction of N as pixel precision error increases. This exercise ignores spatially varying systematic measurement errors that could influence detections.

Figure 1 illustrates that as l_i increases (from left to right panels), plumes from individual point sources cluster into larger plumes, reducing N. This clustering causes the loss of information about the origins of individual plumes from specific point sources, leading to a

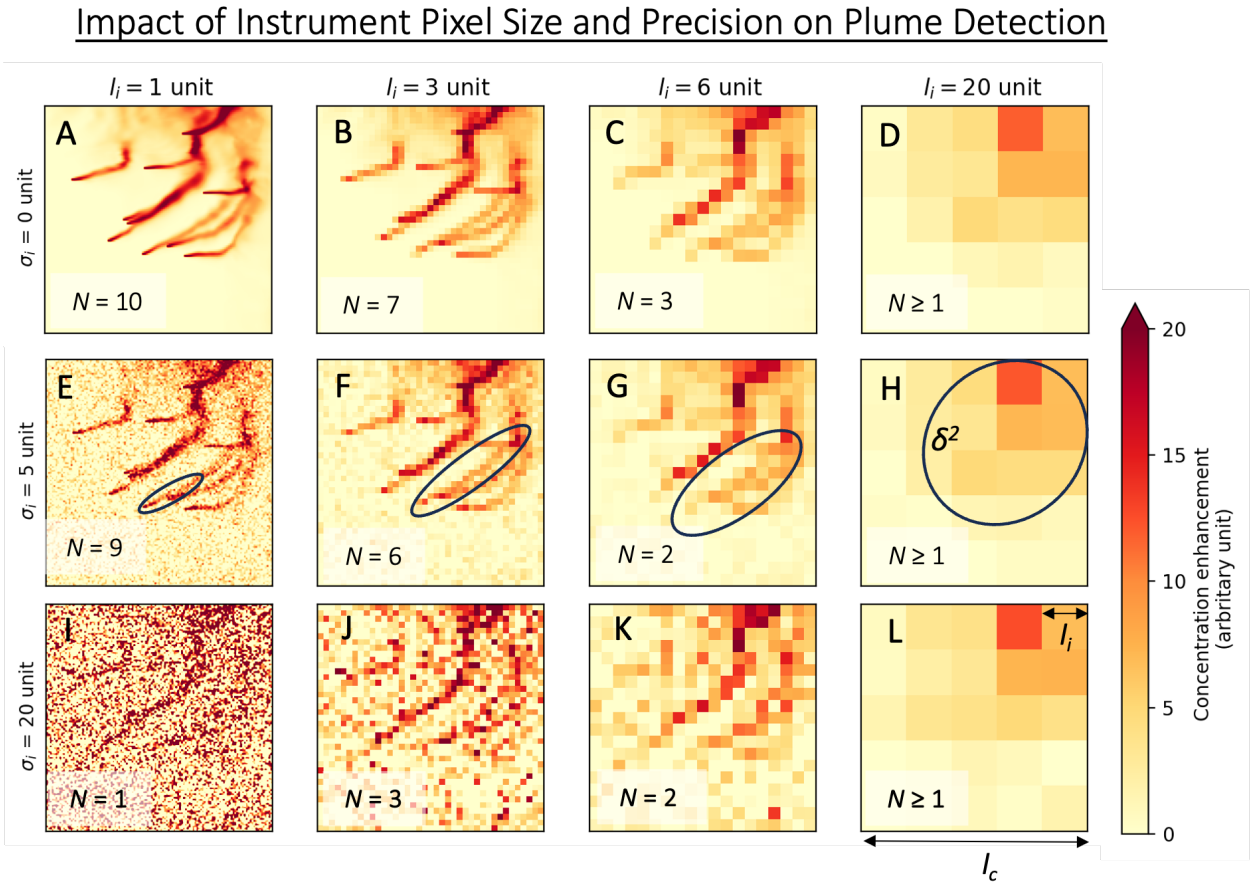

Figure 1: A conceptual illustration of the influence of instrument pixel size l_i and precision error σ_i on plume detection. Panel (A) shows the column-averaged concentration field from a CTM simulation at 1×1 km^2 spatial resolution, featuring plumes from 10 point sources. Each panel represents a coarser (left to right) and/or noisier (top to bottom) version of the same concentration field (Panel A) over the same spatial domain. To simulate pixel precision error, Gaussian random noise with a standard deviation of σ_i is added to the panels in the leftmost column; this precision error reduces due to aggregation across adjacent pixels as we move to the right. N represents the number of distinct plumes identified in each panel. The grid cell size (l_c) and instrument pixel size (l_i) are marked in Panel (L). A rough estimate of emission spatial specificity, δ_i, is given by the area ($= \delta_i^2$) of black ellipses marked in the second row. Note that the units are arbitrary, emphasizing the adaptability of the diagram to a wide range of spatial scales and trace gas plumes. Although the original WRF-Chem CTM run was performed at 1×1 km^2 spatial resolution, this conceptual illustration can be extended to a wide range of spatial resolutions (1 m to 10 km). Our determination of N is inherently subjective, akin to real-world scenarios in which a subjective human decision plays a role in flagging a successful plume detection.

degradation of the emission spatial specificity δ_i. If point sources are densely and uniformly distributed, the number of point sources is proportional to the area, and δ_i degrades proportionally with l_i. The fewer cluster plumes, formed by the merging of smaller plumes, would have higher emission rates. This emission rate boosting also occurs when a plume from a large source masks smaller point sources within its area, as emissions from the smaller sources enhance the concentration of the large plume. Consequently, plume emission rates observed by instruments with different pixel sizes — such as AVIRIS-NG ($l_i = 5$ m), GHGSat ($l_i = 25$ m), Carbon Mapper Tanager-1 ($l_i = 30$ m), MethaneSAT ($l_i > 100$ m), and TROPOMI ($l_i > 5$ km)— will differ. At very coarse resolutions ($l_i = 20$ unit), the instrument loses the ability to identify individual plumes and their sources, although it may still detect the presence of emissions. In such cases, area emission estimation methods—like atmospheric flux inversions and mass balance techniques—can be used to quantify emissions[39,64–67].

As the precision error σ_i increases (from top to bottom panels in Figure 1), the number of plume detections N decreases. Interestingly, with high precision error, it is possible to detect more plumes at coarser resolution than at finer resolution. For instance, in the bottom row of the figure ($\sigma_i = 20$ units), more plumes are detected at spatial scales of $l_i = 3$ and 6 units than at $l_i = 1$ unit. This effect is observed in real-world scenarios. For example, TROPOMI can detect plumes from large areas like cities or wetlands, but when zooming in with fine spatial resolution instruments, a fine-scale plume may not be observed, likely because instrument precision error dominates the plume signal at these finer scales[54].

2.2.2 Impact of Instrument Pixel Size on Emission Rate Distribution of Plumes

A plume instrument's Probability of Detection (POD) function represents the likelihood of detecting a *single* point source plume at a specific emission rate. The POD curve typically has a sigmoid shape (see Figure 2.A): the POD approaches 0 for small point emissions or diffused area sources that create weak plumes (where the concentration enhancement within a pixel is below the instrument's detection capability) and approaches 1 for large point

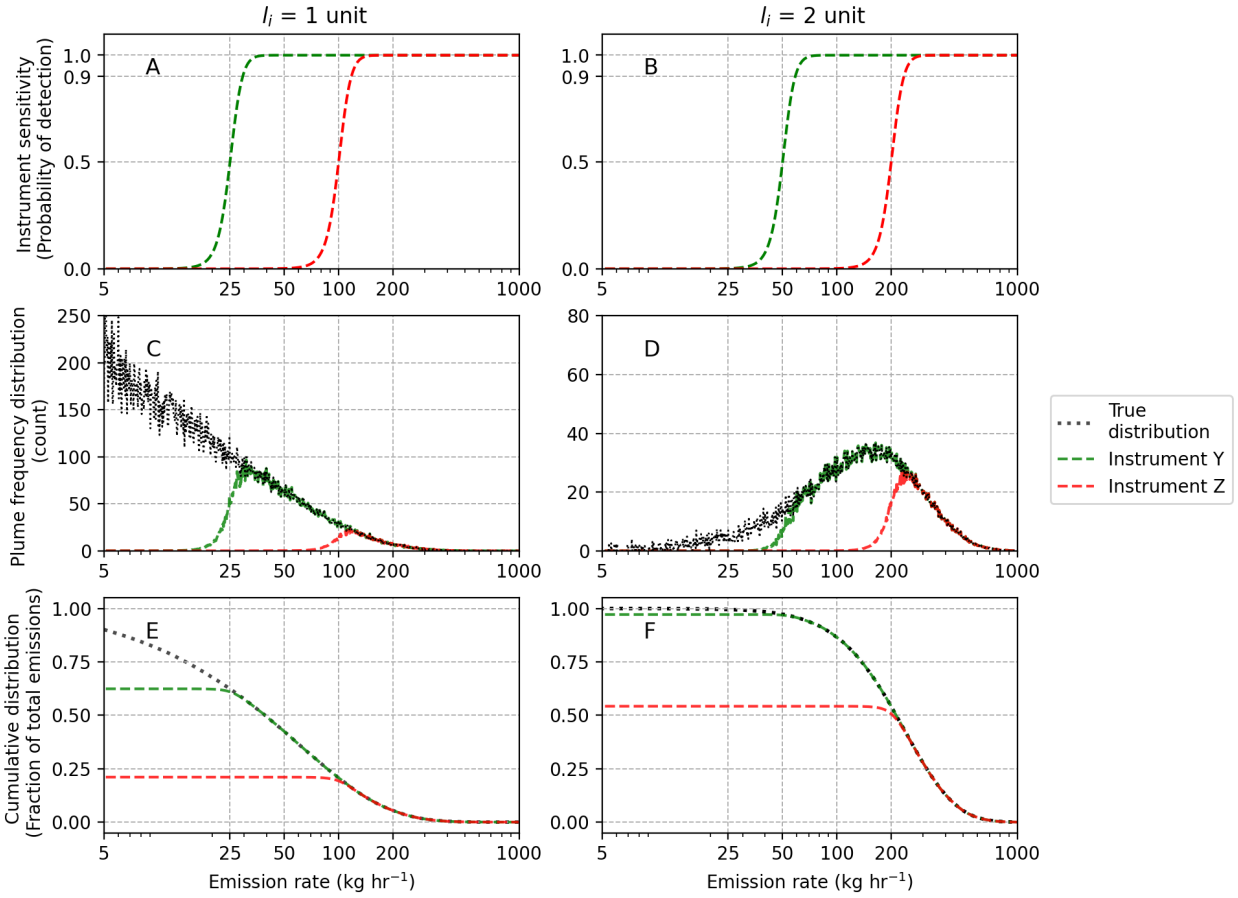

Figure 2: A conceptual illustration of the impact of pixel size on plume emission rate distribution in a hypothetical dense point source emission field. Panel (A) presents the POD curves for two hypothetical instruments, Y (green) and Z (red), each with a pixel size $l_i = 1$ unit. Panel (B) shows the expected changes in POD when aggregating instrument pixels to $l_i = 2$ units. Panel (C) displays the frequency distribution of plume emission rates for $l_i = 1$ unit, showing the true distribution in black and observed distributions for instruments Y (green) and Z (red). Panel (D) shows the frequency distributions for $l_i = 2$ units. Panels (E) and (F) show the cumulative fraction of total emissions observed by the two instruments at the two l_i values.

source emission rates. P_{50} [kg hr^{-1}] of an instrument denotes the emission rate at which the POD value is 50%, meaning half of the plumes at this emission rate will be detected by the instrument. Observation conditions such as surface albedo, solar zenith angle, wind speed, and the detector's altitude impact the POD[55,56]. Surface albedo and solar zenith angle can impact the instrument's SNR, affecting precision error and changing the POD curve. Higher wind speeds may dilute the concentration enhancement per pixel pixels, complicating plume detection.

Figure 2 illustrates how the instrument pixel size affects the emission rate distribution of plume detections in a dense point source field. It highlights the relationship between precision error and resolution by examining changes in plume emission rate distributions. For this conceptual exercise, we assume spatially uniformly distributed point sources, with their emission rates following a Gamma distribution, and that the POD of hypothetical instruments follows logistic functions. Our inferences should remain valid for other reasonable choices of emission rate distributions and POD functions.

Figure 2.A compares the POD functions of two hypothetical instruments. At $l_i = 1$ unit, the P_{50} of instrument Y is 25 kg hr^{-1}, which is four times better than that of instrument Z at 100 kg hr^{-1}. This difference may result from instrument Z having four times higher pixel precision error σ_i than instrument Y. The middle panels of Figure 2 show the frequency distribution of true emission rates (black) from the $l_i \times l_i$ pixels and the corresponding emission rate distribution for the two instruments' plume detections, which is given by the POD curve multiplied by the emission rate distribution.

In the right column of the figure, four pixels are aggregated together. Based on the assumption of our idealized conceptual setup, some notable effects would occur:

1. The P_{50} of the instruments worsens by roughly a factor of 2 due to the combination of two effects:

    - Aggregating pixels dilutes the plume enhancement signal of a point source by roughly a factor of 4.

- Averaging the instrument pixel precision error over four pixels reduces the precision error σ_i by roughly a factor of $\sqrt{4}$.

The net effect is given by the ratio of these two effects, resulting in a worsening of the POD (P_{50} increases) roughly by a factor of 2.

2. The emission signal improves by a factor of 4. A 2×2 pixel group contains four times the point sources compared to a 1×1 pixel, thus increasing the amount of emitted mass per unit time under a pixel.

As the spatial pixel size l_i increases, the number of low-emission group pixels decreases, fundamentally altering the emission rate distribution. According to the central limit theorem, when identically and independently distributed (IID) pixel-wise emissions are summed, the distribution becomes more bell-shaped, with the randomness of individual emissions averaging out, leading to a more symmetric, Gaussian shape. Additionally, the expected value of the emission rate shifts to the right by a factor proportional to l_i^2. Note that the peak of the frequency distribution shifts by the clustering amount only if the distribution is Gaussian (mode = mean); for skewed distributions, the shifts differ.

The bottom panels of Figure 2 display the 'true' and observed cumulative emission distributions, which are normalized relative to the true emission distribution. These cumulative distributions illustrate the fraction of total emissions represented by plumes detected at or above a given emission rate. For instance, Instrument Y can detect nearly 100% of the sum of point source emissions when observing at $l_i = 2$, but only 60% at $l_i = 1$. This highlights the trade-off between spatial specificity and the ability to accurately estimate total emissions at different pixel sizes l_i.

The conceptual exercises in Figures 1 and 2 introduce the concept of clustering and illustrate the trade-offs between detection sensitivity and spatial resolution in instruments. In real-world scenarios, the exact magnitudes of plume clustering will vary from the values presented here, depending on factors such as the spatial distribution of point sources,

pixel size, and the instrument's detection capability. These magnitudes can be empirically estimated by comparing the plume distributions of different instruments. Fine spatial resolution instruments observe a lower fraction of total emissions but provide good emission spatial specificity, offering better information on the location of point sources. Conversely, coarse spatial resolution instruments detect a higher fraction of total emissions but with reduced spatial specificity. The conceptual illustration allows for generalization to include detections by instruments ranging from meter-scale (typically capturing a single point source) to kilometer-scale resolution (typically capturing emissions from a cluster of point sources). In some sense, an area emission observing system is an extreme case of a coarse spatial resolution system, designed to be sensitive to 100% of the total emissions but lacking point source location information.

2.3 Statistical Relationship between Area Estimates and Plume Sums

We present a statistical relationship between area estimates of grid cell emissions—which represent mean emissions over specific spatial and temporal intervals—and the sum of plume emission rates within each grid cell. The complete derivation of the relationship is given in Appendix Section A.1. Several factors must be considered when relating area estimates to plume sums. First, instruments with different pixel sizes (see Figure 1) or detection sensitivities must be treated separately in this relationship. Second, the extent of sampling of the emission field by the plume instrument must be considered, as it determines the number of plume detections and, consequently, the magnitude of plume sums. Third, potential temporal biases in the sampling of the emission field must also be accounted for.

Consider an emission sector or sub-sector category (sector's component), s, within a large grid cell c of area $l_c \times l_c$ [m^2] composed of densely distributed point sources. The area $l_c \times l_c$ can roughly range from 25×25 km^2 (a regional flux inversion grid cell) to more than $5^\circ \times 5^\circ$ latitude–longitude (a global flux inversion grid cell). The time interval associated with c can

be between a week and a year, corresponding to flux inversion periods.

Suppose a plume-detecting instrument i scans different portions of c during a number of scans within the time interval of c. From these scans, plume detections are identified and quantified. Let η_{ic} [unitless] represent the *sampling* of the emission field within grid cell c by instrument i during its time interval. η_{ic} is given by the sum of the ratios of the total of ground areas covered by each of the scans to the grid cell area l_c^2.

Let y_{ics} [mass time^{-1}] denote the sum of emission rates of the plume detections by i in the spatial and temporal extents of c. Let x_{cs} [mass time^{-1}] represent the total emission rate from c of all emissions of sector s . The relationship between y_{ics} and the total area estimates x_{cs} is given by:

$$y_{ics} = \tau_{ics}\kappa_{is}\eta_{ic}x_{cs} \tag{1}$$

Here, κ_{is} [unitless] is a *periodicity bias*, representing the temporal sampling bias of instrument i due to periodic (continuous or intermittent) emissions from sector s, (see Appendix Section A.1). The variable $\tau_{ics} \in [0, 1]$ represents the *plume factor*, which is the fraction of the total emissions from source s that are expected to be observable by sensor i during one complete scan of region c, assuming no periodicity bias. This is defined by $\tau_{ics} = \frac{y_{ics}}{x_{cs}}$, where both $\eta_{ic} = 1$ (indicating full detection by i) and $\kappa_{is} = 1$ (indicating full contribution from s). τ is determined by the instrument's plume detection sensitivity or the POD under the observing conditions of c. Note that in our model, y_{ics} be greater than x_{cs} depending on the amount of scanning of the emission field of c. For instance, consider a hypothetical instrument with $\tau_{ics}\kappa_{is} = 1$. In this case, $y_{ics} = x_{cs}$ for a single complete scan of the grid cell ($\eta_{ic} = 1$), but if the grid cell is completely sampled 20 times by the instrument during the interval of c, then $y_{ics} = 20x_{cs}$.

3 Data

We use plume detections and area estimates of oil and gas emissions in the Permian Basin, USA. Detailed descriptions of these datasets are provided in Appendix Section B. We use plume data collected by two aircraft instruments (ANG and GAO) during the Carbon Mapper campaign in the fall of 2019[53]. The Integrated Mass Enhancement method (IME) was used for the emission quantification of these plumes[31]. The plume data cover a six-week period from September 24 to November 4, 2019. We use the gridded area estimates from two sources: (1) concurrent weekly top-down TROPOMI flux inversions[9] and (2) the annual mean Environmental Defense Fund's (EDF) 2018 bottom-up inventory[68], both at a spatial resolution of $0.25° \times 0.3125°$ latitude and longitude ($\approx 25 \times 25$ km^2).

Following the analysis presented in Sections 2.2.1 and 2.2.2, ANG and GAO are treated as different plume detectors due to significant differences in their observation configurations during the 2019 Carbon Mapper campaign. Their pixel sizes and precision errors differed because the instruments were flown at different flight altitudes. Additionally, their plume detection capabilities were further distinguished as GAO was equipped with a high-resolution visual camera to assist in detecting plumes (see Section B.2). This enhanced plume detection capability of GAO improves its POD and thus affects its plume factors τ.

Figure 3 shows the gridded area emission estimates and the weekly coverage (shown as η) from the two aircraft instruments. η_{ic} represents the sampling of grid cell c by instrument i over the course of a week. Sampling occurred over multiple flight tracks each week. For each flight track j, we calculate the fraction of c covered, denoted by $I(j, c)$. We then compute η_{ic} by summing these grid cell fractions of flight tracks during the week:

$$\eta_{ic} = \sum_{j} I(j_i, c). \tag{2}$$

We estimate the product $\tau_{is}\kappa_{is}$ by taking the ratio of plume sums to the product of TROPOMI area emission estimates and η, both summed across the Permian:

$$\tau_{is}\kappa_{is} = \frac{\sum_{c\in\text{Permian}} y_{ics}}{\sum_{c\in\text{Permian}} \eta_{ic} x_{cs}} \tag{3}$$

Table 1 provides the weekly plume counts, along with $\tau_{is}\kappa_{is}$, and η_{ic} values of the two instruments. $\tau_{is}\kappa_{is}$ values are used in the plume inversions (Section 5.2) and discussed further in Section 6.

Table 1: Weekly statistics of the plume detections by the ANG and GAO instruments of the Carbon Mapper Fall 2019 Permian survey. # is the number of plume detections per week. $\sum_{c\in Permian}\eta_{ic}$ is the sum of weekly grid cell-wise sampling (see Figure 3) of the instruments. $\tau\kappa$ is the plume factor times periodicity bias estimated by taking the ratio between plume sums and area emissions (see Equation 3). $\pm$ denotes one standard deviation spread.

Week	GAO Instrument			ANG Instrument		
	# plumes	$\tau\kappa$	$\sum_{c\in Permian}\eta_{ic}$	# plumes	$\tau\kappa$	$\sum_{c\in Permian}\eta_{ic}$
Sep-27	-	-	-	266	0.68	38.7
Oct-04	-	-	-	318	0.87	22.9
Oct-11	198	1.01	16.9	351	0.7	38.7
Oct-18	187	1.0	20.6	709	0.81	48.6
Oct-25	396	1.05	23.8	310	0.67	29.1
Nov-01	212	0.89	16.7	-	-	-
Mean	250	0.99 $\pm$ 0.06	19.5	402	0.75 $\pm$ 0.08	37.2

4 Empirical Analysis

4.1 Probability Density Functions (PDFs) of Plume Detections

Figure 4 shows the PDFs of weekly plume detections from the ANG and GAO instruments. The two instruments exhibit different PDFs; GAO shows superior plume detection capabilities, identifying more plumes below 30 kg hr^{-1}. The expected values of the weekly PDFs for the ANG plume detections range from 318–485 kg hr^{-1} (mean = 417 kg hr^{-1}), while for GAO detections, they range from 243–443 kg hr^{-1} (mean = 333 kg hr^{-1}). This difference is expected because GAO has better detection sensitivity. GAO operated at an altitude of 4.5 km, resulting in less atmospheric interference and a smaller surface pixel (GAO $l_i = 4.5$

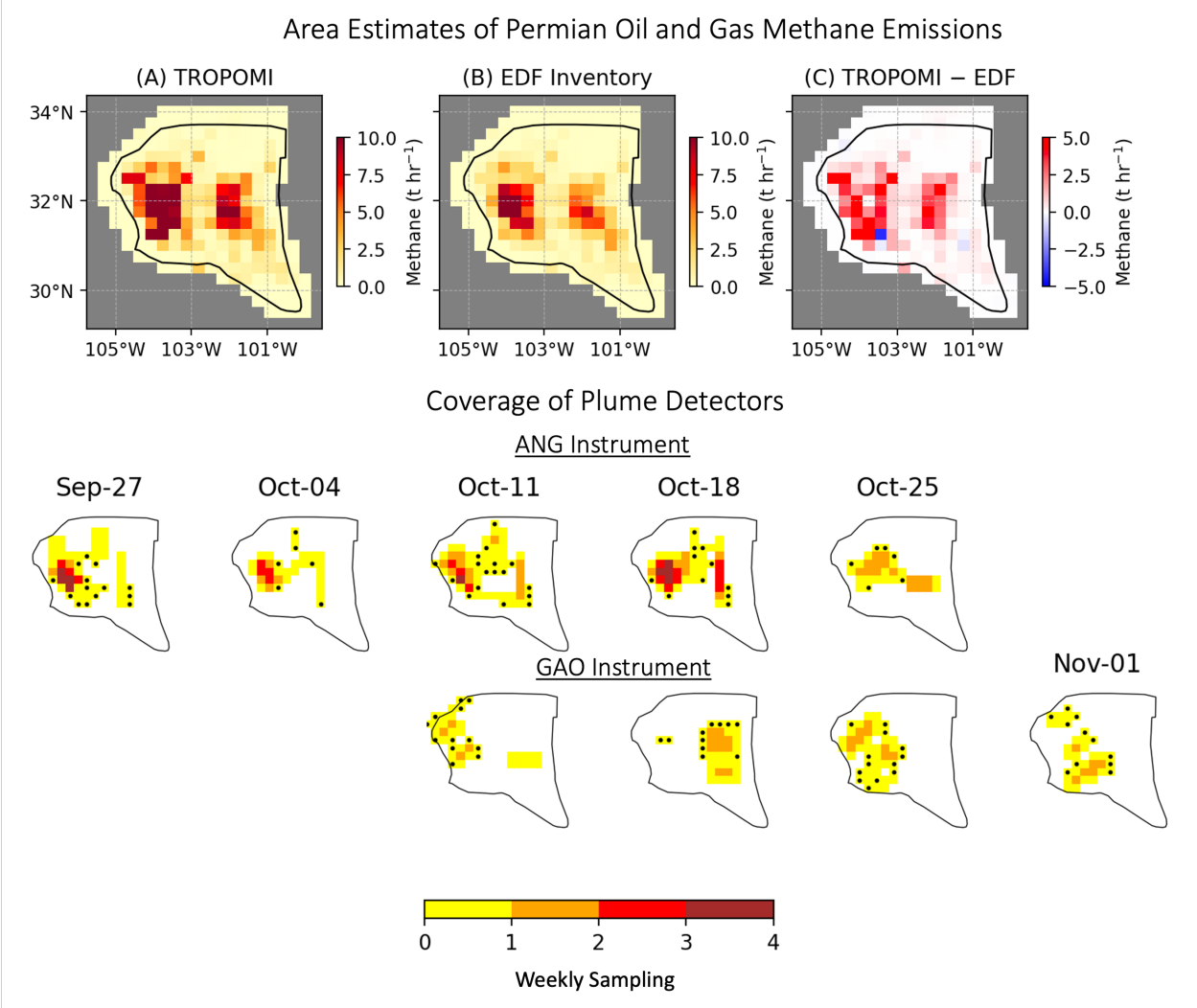

Figure 3: The emissions dataset used in this study. The top row shows the gridded area estimates for the Permian Basin oil and gas emissions from (A) TROPOMI (top-down) flux inversion and (B) EDF (bottom-up) inventory, both at a spatial resolution of $0.25° \times 0.3125°$ latitude-longitude. The EDF inventory was prepared for the year 2018, while the TROPOMI estimates shown here are the six-week (September 24 to November 4, 2019) mean of the flux inversion posterior from Varon et al.[9]. The thick black contour marks the geological extent of the Permian Basin, highlighting two major emissions hotspots corresponding to the Delaware (West) and Midland (East) basins. The middle and bottom rows show the weekly spatial coverage of plume detectors during the Fall 2019 Carbon Mapper survey in the Permian Basin. The sampling factor η for the ANG and GAO instruments is provided for the weekly grid cells of $0.25° \times 0.3125°$ latitude-longitude. η may exceed 1 when a grid cell is observed more than once a week. Black dots indicate cells with $\eta < 0.1$. See also Table 1.

m) compared to ANG, which operated at 8 km altitude (ANG $l_i = 8$ m). Moreover, GAO augmented its plume observations with high-resolution visual imagery to enhance detection accuracy and minimize surface artifacts (see Section B.2).

The standard deviation (SD) of the expected values of the weekly PDFs for ANG is 13% (relative to the multi-week mean). For GAO, the corresponding SD is larger at 28%. The ANG instrument's survey was strategically designed to repeatedly observe regions with high emissions (see Figure 3), whereas the GAO survey aimed to cover the entire Permian Basin at least once. Therefore, GAO encountered a wider range of observation conditions than ANG, resulting in greater POD function variability and expected values of weekly detections.

Figure 4 also displays the 10-meter wind speed data from the High-Resolution Rapid Refresh (HRRR) model, which was used for emission rate quantification of the plumes by Cusworth et al.[53]. Since POD is sensitive to wind speeds[56], the significant variation in GAO's observational conditions is reflected in the weekly wind speed distributions, where the standard deviation of GAO's weekly wind speed expected values is 45%, compared to only 20% for ANG (relative to the multi-week mean wind speeds). The larger variation in GAO's wind speeds results in greater variability in its POD and, consequently, in more diverse plume PDFs. For GAO, there is a noticeable difference between emission rate PDFs and wind distributions between two sets of weeks: the weeks of Oct-11 and Oct-18 differ significantly from Oct-25 and Nov-01. The R^2 between the weekly expected values of the log of wind speed and the log of emission rates is 0.98 for GAO and 0.44 for ANG, suggesting a strong influence of winds on the observed plume PDFs.

Despite the plume detections occurring at different observation locations within the Permian Basin (Figure 3), the shapes of the distributions for GAO and ANG are quite similar across the weeks, with major differences explained by wind speed variations and other spatial factors affecting the POD. After accounting for these variations, we can assume that the PDF of the point source emission rates in the Permian Basin remains strongly correlated over time.

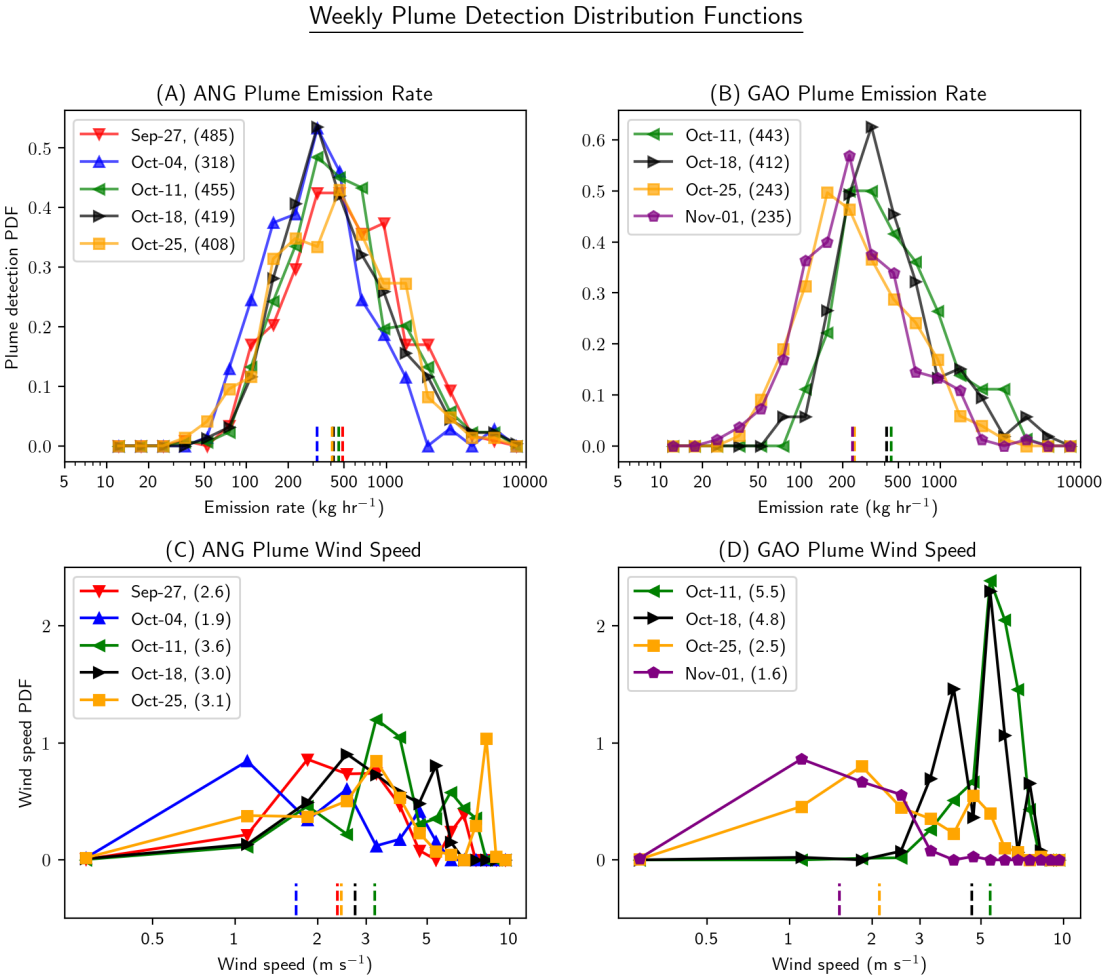

Figure 4: Probability Density Functions (PDFs) of methane plume detections by ANG and GAO aircraft instruments during the Fall 2019 Carbon Mapper survey in the Permian Basin. The top panels display the weekly emission rate PDFs. The bottom panels show the corresponding weekly plume wind speed PDFs. Each line color corresponds to a different week, as indicated in the legends. The emission rates and wind speeds are binned in logarithmic intervals. The expected values of the weekly distributions are given in the legends' parentheses and are marked with the colored vertical lines at the bottom of each panel.

4.2 Comparison of Plume Emission Rate Sums with Area Estimates

We evaluate the relationship between total plume emission rates and area-based emission estimates in the Permian Basin. Figure 5 shows the weekly time series of plume sums and area estimates derived from both the top-down TROPOMI inversion and the bottom-up 2018 EDF inventory. Each area estimate is adjusted for aircraft sampling using η. The 2018 EDF inventory provides only spatial emission patterns for the Permian Basin, and these patterns remain constant each week because the inventory does not include data specific to the six weeks in 2019. However, the temporal variability of the sampling factor η introduces variability into the adjusted area estimates (ηx), as shown in the figure. In the case of TROPOMI, the temporal variability in the time series arises from both sampling and actual emission variability.

We observe strong correlations between plume sums and concurrent top-down area estimates, with GAO achieving $R^2 = 1.0$ (P = 0.001) and ANG reaching $R^2 = 0.95$ (P = 0.005). In contrast, when comparing plume sums to the temporally constant EDF estimates, the correlations are lower: GAO $R^2 = 0.84$ (P = 0.09) and ANG $R^2 = 0.59$ (P = 0.13). These overall high correlation values demonstrate that Equation 1 effectively relates area estimates to plume sums across large spatial domains such as the Permian Basin.

Figure 6.A presents the R^2 values between area estimates, plume counts, and plume emission rate means. The mean of plumes correlates negligibly with area estimates ($R^2 \leq 0.26$ for both EDF and TROPOMI). For GAO, R^2 goes up to 0.26, but it has a high uncertainty, as indicated by a high P value (P = 0.51). The strong correlation with plume sums but negligible correlation with plume means implies that there should be a correlation between the number of plume detections and area estimates. This hypothesis is also supported by the empirical tests (R^2 range of 0.31–0.78 for top-down).

Figure 6.B presents the R^2 values at the grid cell level ($\eta_{ic} x_{cs}$ vs. y_{ics}). As anticipated, R^2 diminishes at smaller spatial scales due to increased noise. For plume means, R^2 is negligible for both bottom-up and top-down estimates. The plume sum R^2 values with the bottom-up

EDF inventory are $R^2 = 0.63$ and 0.44 for ANG and GAO, respectively, surpassing those with the top-down TROPOMI, where the respective R^2 values are 0.58 and 0.32 ($P < 1^{-15}$ for all grid-scale plume sum R^2). ANG shows a stronger correlation with area emissions at the grid scale, likely because it samples the emissions field more extensively by repeatedly observing high-emission areas under more consistent conditions than GAO. As a result, individual data points for ANG's have lower relative noise. In contrast, GAO includes pixels with very low emission activity where noise can dominate because it samples areas away from major emission sources in the Permian basin.

The poor correlation between plume means and area emissions can be explained as follows: The plume PDFs are independent of emission activity factors. While area emissions, plume sums, and plume count all scale with activity factors, plume means do not (see the equation in Appendix Section A.1). When wind speed variability is introduced, it adds additional variability to all three plume quantities. For plume sums and plume counts, wind speed variations introduce noise, potentially slightly reducing the correlation with area estimates from the ideal value of 1. In the case of plume means, starting from an expected correlation of zero under ideal conditions, wind speed variability could theoretically introduce random fluctuations that might increase the observed correlation with area estimates. However, wind speed fluctuations over weeks are uncorrelated with total area emissions or activity factors, keeping the correlation between observed plume PDFs and area estimates near zero.

In our analysis, we presented results at two spatial scales: basin total and grid cells. While the correlation is lower at the grid cell level compared to the basin total due to increased noise, it remains strong (for instance, R^2 of roughly 0.6, with $R \sim 0.77$, for ANG plume sum versus both EDF and TROPOMI). These good correlation values indicate that plume sums align well with area estimates even at the grid scale. The correlation is expected to improve even further when grid cells are aggregated.

The errors in plume sums, EDF inventory, and TROPOMI estimates are expected to be

independent when representing true emissions. In the quasi-Kalman-filter approach of Varon et al.[9], the posterior estimates are nearly independent of the EDF inventory prior, which is used only for the first week of the multi-year inversion. Given the independence among the three estimates, if any two of them agree while the third does not, it suggests that the first two are closer to the truth. A poorer correlation of plume sums with TROPOMI flux inversions at the grid cell level suggests that the EDF bottom-up inventory and plume data have superior spatial information at fine scales. This also indicates that TROPOMI is less effective at high spatial resolutions for constraining emissions, likely due to limitations in the CTM and TROPOMI coverage and resolution. In contrast, the better agreement between TROPOMI and plume data shows that the TROPOMI inversion's total weekly emission estimates for the Permian are better than those from EDF. Assimilating plume sums can be a promising approach to improve the fine-scale features in flux inversion estimates. This will be explored further in Section 5.2.

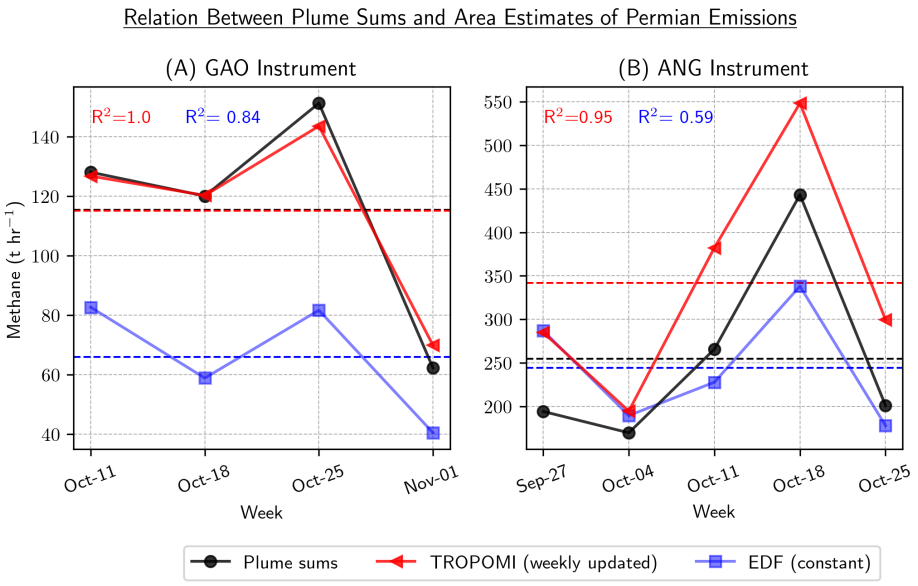

Figure 5: Comparison of time series of weekly plume emission sums ($= \sum_{c \in \text{Permian}} y_{ics}$) and area emission estimates. The top-down area estimates (concurrent weekly TROPOMI flux inversion) are shown in red, and bottom-up area estimates (annual 2018 EDF inventory) are shown in blue. The area estimates are adjusted for instruments' sampling ($= \sum_{c \in \text{Permian}} \eta_{ic} x_{cs}$). The R^2 between area estimates and plume sums are given in the respective colors. The dashed horizontal lines mark the means of the time series.

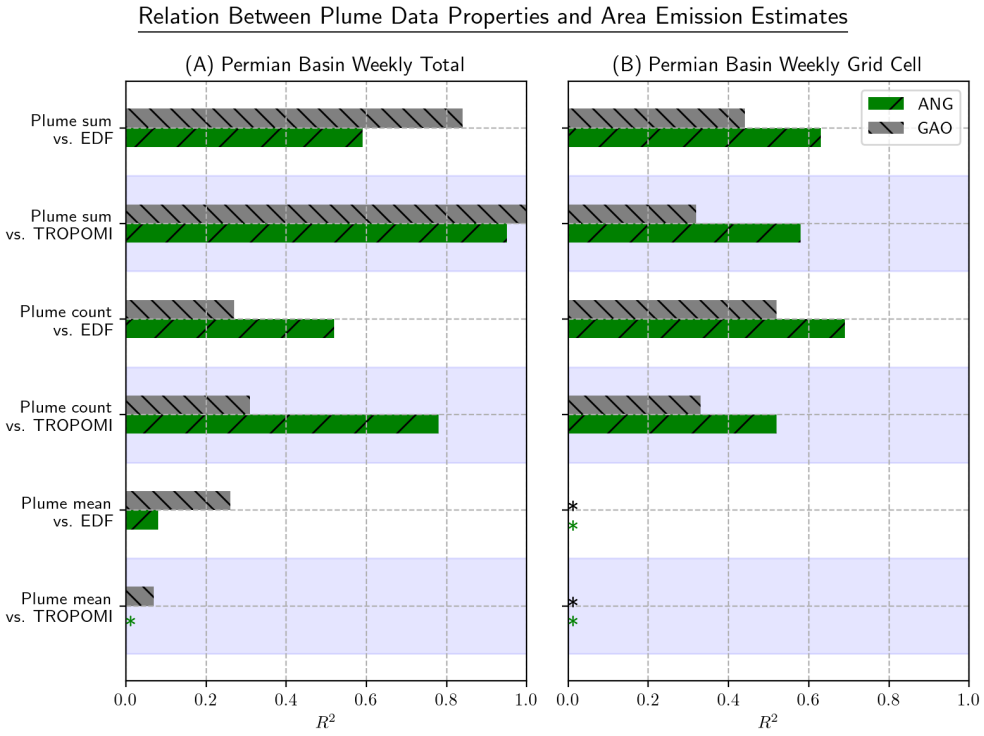

Figure 6: Correlation (R^2) between properties of weekly plume detections and sampling-adjusted area estimates. Panel (A) shows the correlation for the weekly aggregate over ($\sum_{c\in\text{Permian}} \eta_{ic} x_{cs}$ vs. $\sum_{c\in\text{Permian}} y_{ics}$). Panel (B) shows the correlation at the grid cell level ($\eta_{ic} x_{cs}$ vs. y_{ics}). The plot compares the plume emission rate means, sums, and the number of plumes (count) with top-down (TROPOMI, light-blue shaded regions) and bottom-up (EDF) area estimates. Green bars represent ANG data, while gray bars represent GAO data. R^2 values of < 0.02 are marked with "*".

4.3 Correlation of Plume PDFs

Our empirical analysis shows that the mean of plume emission rates does not correlate with area estimates for a sector across space and time. However, the sums of emission rates—and, to a lesser extent, the number of plume detections—exhibit a strong correlation with area estimates. These empirical observations can be explained by the hypothesis that the true PDFs of point source emission rates within a sector are highly correlated in space and time, remaining nearly invariant over regional spatial and temporal intervals, such as the Permian Basin emissions over several weeks. In Figure 4, we showed that variations in the observed plume PDFs—and their expected values of observed plume detections—are predominantly driven by changes in the instrument's POD, including fluctuations in wind speeds.

The spatial and temporal correlation of point source PDFs can be physically explained as follows. The distribution of point source emissions within a sector depends on (1) the proportions of different components (e.g., valves, small pipes, large pipes, wellheads, etc.) and (2) the maintenance and quality of emission-causing components. These factors correlate because they are shaped by technological, economic, and regulatory contexts, which exhibit spatial and temporal correlations. Therefore, the point source PDF for a sector in a given region is determined by the proportions of components and their respective emission PDFs[37]. Consequently, point source PDFs for sectors like oil and gas within a unified administrative boundary, such as the Permian Basin, are expected to be similar. Plume PDFs are likewise correlated because they represent spatial aggregations of point source emission PDFs at the emission spatial specificity of the plume-detecting instruments (see Section 2.2.2). Different administrative and economic regions, such as oil and gas operations in Turkmenistan versus the Permian Basin, can exhibit very different PDFs. For instance, Turkmenistan has a significantly higher number of large emitters exceeding 1000 kg hr^{-1}[69].

5 Applications

5.1 Evaluating Area Estimates Using Plumes

Evaluating the accuracy of area estimates from flux inversion and bottom-up inventories poses several challenges. The inversions constrain total emissions from various sources across large areas. The area estimates are typically evaluated against atmospheric concentration measurements from in situ and TCCON sites, using a CTM to simulate atmospheric concentrations resulting from the emissions. However, errors in the CTM are a major component of the overall flux inversion errors[25–27]. Consider a scenario where both the assimilation observations and the validation data used in inversions are accurate, but the inversion relies on a CTM that contains errors. These CTM errors will propagate into the emissions estimates when the inversion attempts to match the observations by adjusting the emissions. Since the

observation and validation data are consistently accurate, the simulated posterior field will still agree with the data. Therefore, evaluating inversion estimates using CTM simulations may not reveal CTM-related errors in emissions.

The previous section showed that plume sums strongly correlate with area estimates. This strong correlation enables the use of plumes to evaluate area estimates. The discrepancy between the correlation of plume sums with temporally variable top-down and constant bottom-up emissions can provide insights into the ability of plume observations to evaluate temporal variations in area emissions. We define a metric ϕ_T called the *plume temporal sensitivity* to measure this ability.

$$\phi_T = R^2_{\mathrm{TS}} - R^2_{\mathrm{S}}. \tag{4}$$

Here, R^2_{TS} is the correlation of plume sums with area estimates that have both temporal and spatial variations, while R^2_{S} is the correlation with area estimates that are constant in time and only have spatial variation. Subtracting the correlation with constant emissions removes the R^2 dependence on the spatial patterns of emissions and the sampling factor η.

We use the correlation of plume sums with TROPOMI and EDF as R^2_{TS} and R^2_{S}, respectively, to test the capability of the ANG and GAO plumes. The value of ϕ_T is 0.36 for ANG and 0.16 for GAO (the difference between the R^2 for TROPOMI and EDF in Figure 5). The modest ϕ_T for GAO is likely due to its lower sampling (993 plumes over 4 weeks) of the emission field and greater variations in observation conditions. In contrast, ANG performed repeated observations in the emission-dense regions of the Permian Basin, leading to a detection count of 1954 plumes over 5 weeks, approximately double the number detected by GAO.

An important implication of our PDF correlation assertion (Section 4.3) is that plume instruments with detection sensitivities poorer than those of ANG and GAO should also be capable of predicting variations in area emissions. Assuming the full point source PDF

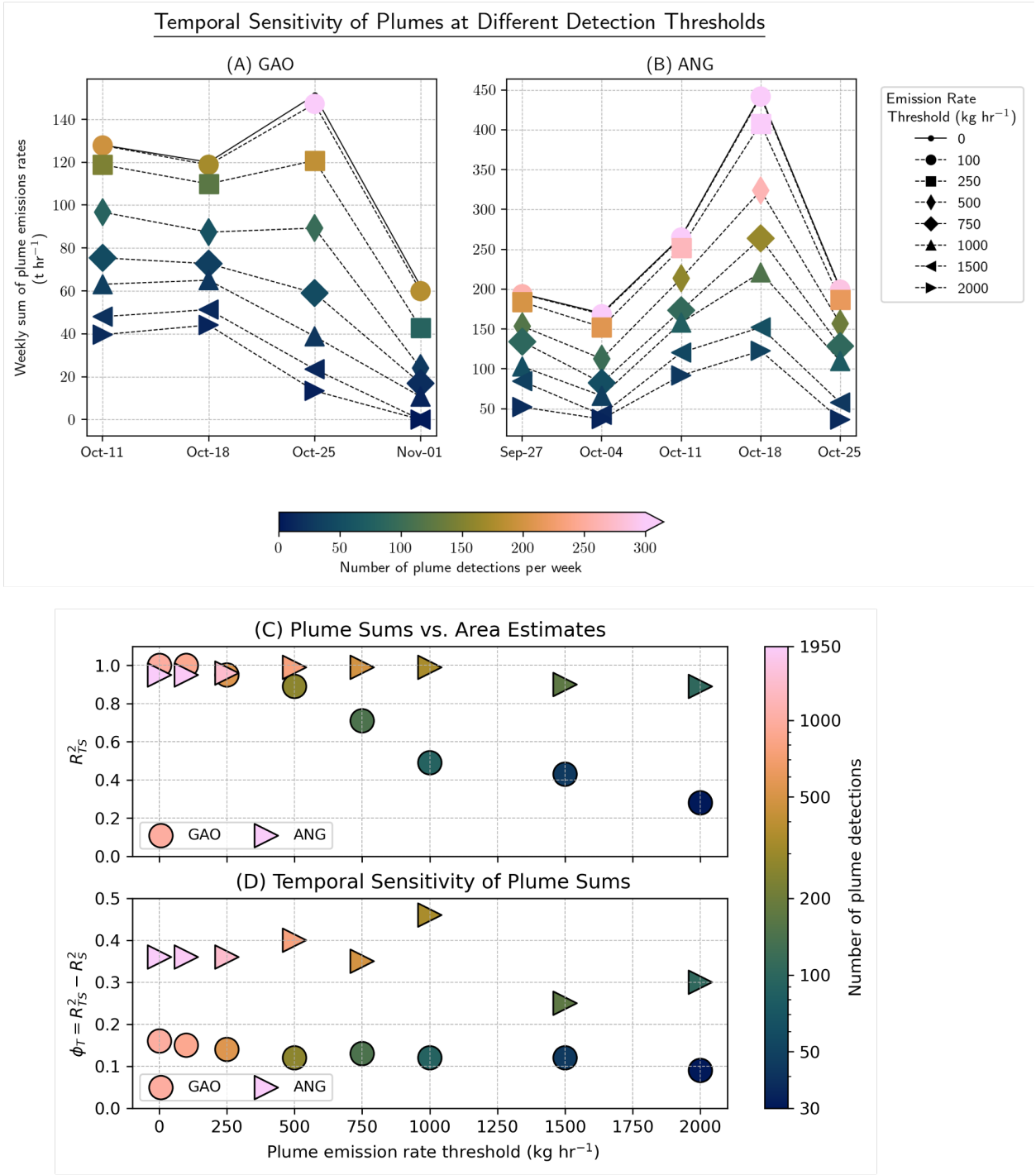

Figure 7: Temporal sensitivity of plume detections to area emissions at various emission rate thresholds. The panels in the top row show the weekly sum of detected plumes from oil and gas emissions in the Permian Basin for the GAO (A) and ANG (B) instruments. Plumes are filtered based on different emission rate thresholds, with plumes below each threshold discarded. Marker colors represent the number of plumes detected each week above the given emission rate. Panels (C) and (D) further explore the relationship between plume sums and area estimates of emissions. Panel (C) illustrates the R^2 values for the correlation between the sum of plume detections and top-down TROPOMI flux inversion estimates for both GAO and ANG. Panel (D) presents the temporal sensitivity (ϕ_T) of plume sums as a function of the emission rate threshold, indicating how sensitive the detected plume sums are to different detection thresholds. In Panel (C) and (D), the colors denote the total number of plumes over the 6-week period.

and POD of an instrument remain stable for a sector and region, the tail of the PDF observed by an instrument with poor sensitivity can still constrain total area emissions. Consequently, the sum of the tail of the frequency distribution of detected plumes scales with area estimates (Appendix Equation 6), showing that both plume frequency distribution and area estimates scale with activity, and therefore, with each other. The 50% POD, P_{50}, for the ANG and GAO instruments used in the Permian survey ranges from 50 to 300 kg hr^{-1} [29,55]. In comparison, most satellite instruments are expected to have poorer detection sensitivities with P_{50} around 1000 kg hr^{-1} (although satellites can identify plumes well below 100 kg hr^{-1} under favorable observation conditions). Figure 7 shows the temporal distribution of the plume sums from ANG and GAO after applying different emission rate thresholds, excluding detections below each threshold and including fewer plumes with high emission rates. The overall shape of the weekly sum time series remains similar, even when a threshold of 2000 kg hr^{-1} is applied, which is the sensitivity of Sentinel-2 and Landsat instruments[51,70]. To test this hypothesis, we evaluated R^2 correlations between TROPOMI and plume sums while only considering plumes above a certain detection threshold.

Figure 7.C shows the correlation between area and plume sums after applying emission rate thresholds. For the ANG instrument, starting with a zero threshold $R^2_{\mathrm{TS}} = 0.95$ with 1954 plumes, R^2_{TS} remains stable at 0.88, even with large thresholds up to 2000 kg hr^{-1} and only 103 plumes remaining. For the GAO instrument, $R^2_{\mathrm{TS}} = 1$ at zero emission rate threshold, but it shows a marked decline after a 750 kg hr^{-1} threshold, with only 143 plumes remaining. Notably, an R^2_{TS} of 0.28 is maintained even with 29 GAO plumes at the 2000 kg hr^{-1} threshold. The sharp decrease in R^2_{TS} for GAO at high thresholds can be attributed to the low sampling of GAO, resulting in fewer plume detections and more diverse observational conditions encountered by GAO.

Figure 7.D shows the temporal emission sensitivity metric ϕ_T. We find that ϕ_T is mostly independent of the emission rate thresholds. Surprisingly, ϕ_T for GAO remains stable across thresholds even though the R^2_{TS} values drop. The likely cause is that the errors added to

the GAO plume sum time series with a lower number of plumes are uncorrelated with area emission variability. Therefore, the errors affect R^2_{TS} and R^2_{S} similarly, and the difference between the two remains unchanged. Overall, our analysis shows that satellite plume instruments, despite their lower detection sensitivity, can evaluate area estimates of oil and gas sector emissions. Our findings align with Lauvaux et al.[71] and Ehret et al.[51], who proposed that detected plume emission rates follow consistent global and regional patterns.

5.2 Bayesian Plume Inversion

Current atmospheric flux inversion methods utilize satellite or in situ concentration observations in conjunction with a CTM to inform grid-scale area estimates. Plume detections provide independent emission observations that can enhance these area estimates. Here, we perform Bayesian assimilation of gridded plume sums (referred to as *plume inversion*) on grid cell area estimates using the plume sum model (Equation 1).

5.2.1 Plume Inversion Setup

We provide a brief summary of the methodology here, with detailed plume inversion methods in Appendix Section A.2. The plume inversions optimize a state vector representing weekly area estimates between September 24 and November 4, 2019, on a 25 $\times$ 25 km^2 grid within the Permian Basin, focusing on the oil and gas sector. Each week, 235 state vector elements are optimized. We refer to the plume inversions as Plume-EDF inversion and Plume-TRO inversion that respectively use EDF and TROPOMI emission estimates as priors. The maximum a posteriori (MAP) solutions are termed Plume-EDF and Plume-TRO estimates. As per Equation 1, the weekly plume factor times periodicity bias ($\tau\kappa$) and temporal sampling (η) are needed to link area estimates with plume sums. Table 1 presents the weekly values of $\tau\kappa$ and η. A single $\tau\kappa$ value is used for each instrument in both inversions because $\tau\kappa$ is a property of the instrument and emission sector. Assuming TROPOMI mean emission estimates are closer to the truth, the $\tau\kappa$ value is averaged from weekly TROPOMI and plume

data comparisons.

5.2.2 Weekly Total Permian Emissions

Figure 8 shows the total weekly emission estimates from the plume inversions. Degrees of Freedom for Signal (DOFS) values in the figure represent the magnitude of observational constraint provided by the plumes in the inversion (Equation 15). For both inversions, the weeks with large DOFS (Oct-11, Oct-18, Oct-25) coincide with the periods when both GAO and ANG instruments were surveying (see Figure 3). During these weeks, the DOFS ranges from 30–38. In the other three weeks, when only one instrument was surveyed, the DOFS ranged from 13–21.

The Plume-TRO inversion's adjustment to the TROPOMI prior is minor overall, resulting in an increase of 3% over a 6-week mean (from 462 ± 8 to 472 ± 7 t hr^{-1}). This outcome is expected, given that TROPOMI prior emissions serve to anchor the plume constraint, with $\tau\kappa$ quantified from TROPOMI estimates (see Equation 3). On a weekly basis, a substantial 13% adjustment is noted for the week of Oct-11 (from 455 ± 23 to 513 ± 18 t hr^{-1}) in the Plume-TRO inversion. Other weeks exhibit smaller adjustments, ranging from -5% to $+6\%$. During the week of Oct-11, the flux inversion by Varon et al.[9] had the lowest DOFS (2.2 for a state vector with 235 elements), indicating insufficient constraint on the emissions by TROPOMI data. In contrast, other weeks displayed higher DOFS values in Varon et al.[9]'s inversion (2.3–8.3). A common reason for low DOFS is a low amount of TROPOMI observations due to the presence of clouds, etc. The fact that the most significant adjustments in Plume-TRO inversions occur when TROPOMI estimates are most uncertain suggests that plume observations improve the accuracy of area emission estimates for this week.

Significant adjustments are observed in the Plume-EDF inversion, with plume assimilation increasing the 6-week mean emission rate by 30% (from 294 ± 16 to 380 ± 9 t hr^{-1}). The inversion aligns the posterior Plume-EDF more closely with TROPOMI (and Plume-TRO)

estimates, reducing the initial 36% underestimation to 18%. This improvement to the mean is expected, as TROPOMI estimates anchor the plume constraint. Weekly adjustments to the prior EDF inventory are more interesting. Despite using a single $\tau\kappa$ value each week, plume assimilation consistently weekly aligns emissions with TROPOMI estimates, especially during periods with high DOFS. For the week of Sep-27, TROPOMI estimates align with the EDF, and the DOFS is minimal, resulting in negligible adjustments by the Plume-EDF inversion. Conversely, during the week of Nov-1, despite much larger TROPOMI estimates, the low DOFS (17) in the Plume-EDF inversion leads to insignificant adjustments. Excluding the week of Nov-1, the plume inversion improves the R^2 from 0 (constant EDF estimates) to 0.79 (P = 0.04). Our analysis demonstrates that plume data can significantly enhance the accuracy of regional total area emission estimates.

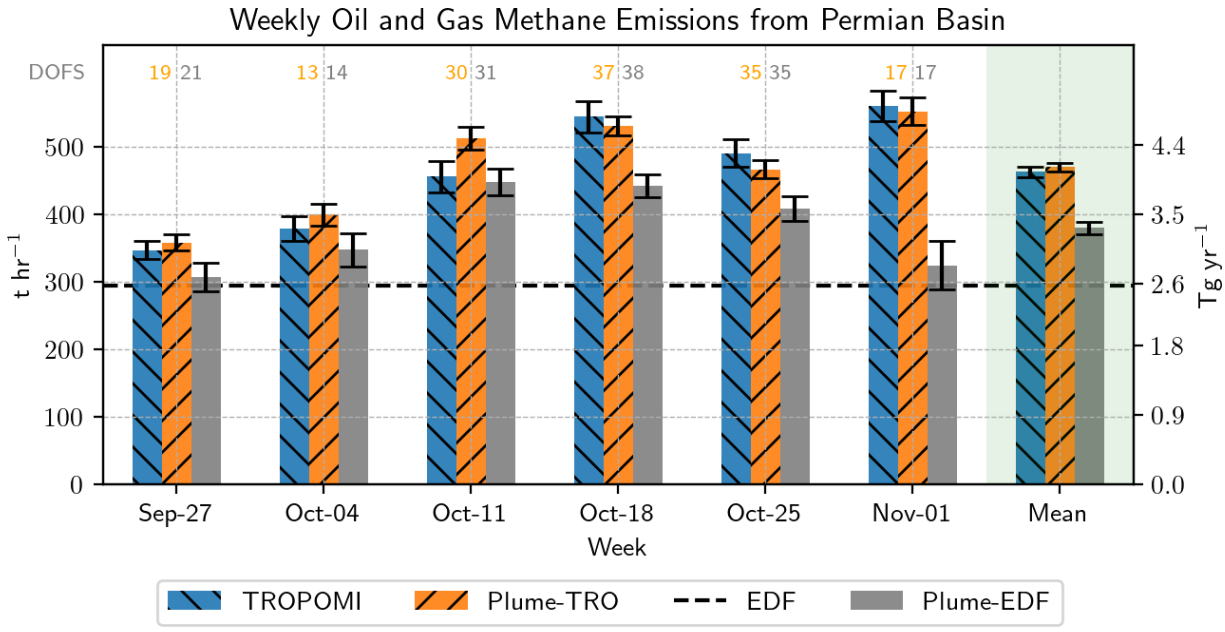

Figure 8: Weekly methane emission estimates for the Permian oil and gas sector. The dashed horizontal line represents the EDF inventory. 'TROPOMI' and 'Plume-TRO' denote the prior and posterior for the plume inversion performed on TROPOMI emission estimates, respectively. Similarly, 'EDF' and 'Plume-EDF' represent the prior and posterior for the EDF plume inversion. The DOFS values (orange for Plume-TRO inversion and gray for Plume-EDF inversion) above each bar indicate the level of observational constraint in the inversions. The right-most group of bars gives the mean values across the weeks. Error bars indicate one standard deviation uncertainty.

5.2.3 Spatial Patterns

Figure 9 shows the mean grid-scale emissions for the Plume-EDF and Plume-TRO inversions. The Plume-EDF inversion increases the emissions in most of the grid cells, and the magnitude of emissions becomes similar to the TROPOMI estimates. Both inversions have DOFS hot spots following the spatial pattern of the two major oil and gas production regions: the Delaware (West) and Midland (East) Basins. This is expected, as the plume surveys targeted these major oil and gas production regions. The plume inversion also improves (reduces) the cross-correlation among area emission grid cells (see Appendix Figure 11). Flux inversions assimilating concentration data induce cross-correlations between grid cells across spatial, temporal, and sectoral domains due to the limitations in resolving the sensitivities across multiple grid cells, often constrained by limited observational data or the resolution of CTM. Given plumes' near-perfect spatial and sectoral attribution, their assimilation reduces the off-diagonal elements of the correlation matrix, enhancing the spatial specificity of the area emission estimates.

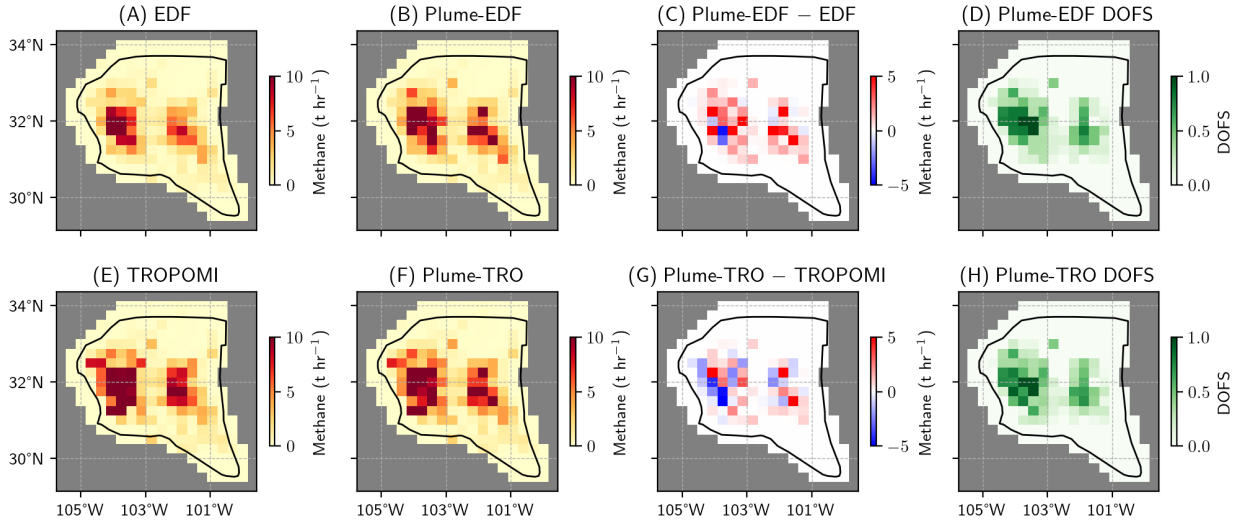

Figure 9: Six-week mean grid-scale emission maps from plume inversions. Panels (A) and (E) display the priors used in the two inversions, respectively. Panels (B) and (F) show the posterior emissions resulting from the plume inversions, while Panels (C) and (G) show the updates made by the plume inversions. Panels (D) and (H) depict the Degrees of Freedom for Signal (DOFS) per pixel, indicating the observational constraints provided by plume data over the six-week period.

6 Discussion

6.1 Plume Constraint on Area Emissions Estimates

The plume data record is expanding rapidly, with plumes now regularly observed by numerous aircraft and satellite instruments[72]. We have presented a method to utilize plume detections to evaluate and inform total regional emission estimates. Our approach benefits flux inversion and bottom-up modelers in several ways. First, our approach represents a no-cost gain on the existing area estimation infrastructure. Plume detections, primarily employed for Leak Detection and Repair (LDAR) methods, thus become a cost-effective option for providing additional top-down constraints on area estimates. Conversely, data from non-imaging concentration satellites like the Greenhouse gases Observing SATellite (GOSAT) are mostly used for flux inversions. Second, plume detections provide fine spatial, temporal, and sectoral specificity, a feat particularly challenging for conventional top-down methods, which rely on limited-resolution numerical approximation of chaotic atmospheric transport. Third, plume detections provide information on the emission processes, especially in identifying anomalous emissions and their contributions to total emissions, which can improve bottom-up estimates[8,37].

Our study has focused on plume detection from imaging instruments onboard aircraft and satellites. Many surveys use on-ground or aerial in situ instruments to estimate component or facility-scale emissions[1,73–75]. These emission datasets have very similar properties to the aircraft and satellite plume datasets from imaging instruments as they provide location, time, and emission rate estimates. The gridded sum of such in-situ-based plume datasets can also be used to evaluate area estimates or in a plume inversion.

Note that plume-based evaluation of area emission estimates and the plume assimilation presented here does not require estimating the full PDF of the plumes (or point sources). The evaluation of temporal variability in area estimates only requires accounting for η. For plume assimilation, the product $\tau\kappa$ factor needs to be considered additionally. An estimate

of $\tau\kappa$ can be obtained by directly comparing the area emissions from a reliable top-down inversion and the sum of plume emissions after accounting for the sampling factor η, as shown in this study.

A key goal of our study was to develop and validate a theory linking plume detections to area emission estimates. By applying this theory to six weeks of data from the Permian Basin under ideal conditions, we demonstrated the potential of assimilating plume data to improve emission estimates. Our analysis advances the understanding of emissions observation methods and lays the groundwork for future applications, although additional factors may need to be considered when applying the theory to other emissions sectors and regions worldwide. Our study focused on the oil and gas sector, characterized by numerous small leaks rather than a few large sources. Extending this approach to other sectors, such as waste management, requires understanding the relationship between plumes and area emissions in those contexts, necessitating further theoretical and empirical analysis.

The effectiveness of plume data assimilation in constraining oil and gas emissions will depend on the availability of plume observations. With the launch of new satellites from GHGSat and Carbon Mapper, as well as the recently launched MethaneSAT and EMIT instruments, the volume of plume data is increasing, enabling more regions to be effectively constrained. Advances in data processing algorithms are also enhancing plume detection capabilities; for instance, recent studies have shown that Sentinel-2, utilizing machine learning across all spectral bands, can detect numerous plumes below 1 t/hr by distinguishing methane signals from surface albedo variations[70]. We anticipate that the detection limits of other instruments with underutilized spectral information will also improve. Nonetheless, within a Bayesian framework, even limited plume data can contribute to constraining area emission estimates if model and data uncertainties are properly accounted for. The low amount of plume observations will result in weaker constraints, which will be reflected in larger posterior uncertainties and low DOFS.

We acknowledge that many regions may have insufficient plume observations to effectively

constrain area estimates. This limitation is not unique to plume data; it also affects CTM-based flux inversions due to a lack of concentration data in tropical regions caused by cloud cover and at high latitudes. Evaluating flux inversion estimates using plume data, even from occasional aerial or in situ surveys, can test flux inversion estimates.

6.2 Co-assimilation of Plume and Concentration Data

Our plume inversion method provides an approach for using fine-spatial-scale plume information from concentration imaging instruments to constrain area emissions. Almost all methane-concentration-imaging area mappers observe methane plumes[52]. For example, TROPOMI methane plumes have been detected from single point sources[54,71] and clusters of point sources[50].

Using our plume inversion approach, the co-assimilation of plume and area information is particularly relevant for new and upcoming imaging satellites that will provide concentration constraints and detect plumes with small spatial pixels. The recently launched MethaneSAT satellite instrument has a pixel size of 100 meters by 400 meters and a 200-kilometer swath[76]. The proposed Carbon-I NASA Earth System Explorer mission will observe at a 400-meter spatial pixel in normal (non-target) operation mode[77]. These instruments will detect methane plumes and provide top-down concentration constraints for flux inversions. Suppose a CTM with 25×25 km^2 spatial resolution is used in an inversion assimilating the 400-meter pixel observations. In that case, the inversion cannot use any concentration gradient information finer than 25×25 km^2. The plume inversion approach can maximize the use of information from these satellite observations to inform area emission estimates.

6.3 Periodicity of Permian Oil and Gas Emissions

Some studies have investigated the extent to which area estimates can be accounted for by plume detections[5,29,53,57,58], while others have attempted to estimate country-scale emissions using point sources within the oil and gas sector in the USA[6,8,42] and across basins[36,37].

These studies utilize plume detections to refine emission factors and employ a bottom-up extrapolation approach assuming persistence characteristics. However, the temporal bias of plume detection emissions is not always accounted for, which can potentially result in the overestimation of emissions. Oil and gas production emissions have been shown to exhibit significant periodicity due to activities such as manual liquid unloading and maintenance operations, which typically occur during afternoon working hours [57,74]. Consequently, instruments that favor afternoon observations are likely to exhibit overestimation.

Our analysis indicates a diurnal periodicity in the Permian Basin oil and gas emissions, shown by the high values for the product of plume factors and temporal bias (weekly $\tau\kappa$ range 0.89–1.05 for GAO instruments). Theoretically, $\tau \leq 1$. We expect true τ to be around 0.5 for the AVIRIS-NG (a combination of GAO and ANG) in the Permian Basin, considering Kunkel et al. [29] showed that many small plumes are not detected by AVIRIS-NG. The observed $\tau\kappa$ can only be explained by $\kappa > 1$. Even though TROPOMI observes during the afternoon, region-scale TROPOMI inversion estimates are expected to have a smaller temporal bias since they are sensitive to emission history from the past hours/days. It is possible that our $\tau\kappa$ estimates may be high due to the underestimation of Permian emissions by TROPOMI inversion.

We advocate for future studies to consider emission periodicity when calculating mean emissions using daytime instruments. Periodicity bias can be assessed with bottom-up data or through an optimal plume survey strategy. For example, continuous day-night monitoring in the Permian Basin using aerial LIDAR or in situ instruments could capture emission periodicity.

6.4 Comparison of Plumes from Different Instruments

Our work highlights challenges in comparing plume emission rates from instruments with different pixel sizes, especially in dense emission fields like oil and gas basins. Coarser pixel instruments capture emissions from more point sources, complicating direct comparisons

without accounting for smaller sources (Figure 1). We demonstrated how pixel size affects observed plume emission rates (Figure 2).

Kunkel et al.[29] estimated the POD curve for the AVIRIS-NG instrument using LIDAR plume detections, noting that differing spatial resolutions could introduce biases. They aggregated LIDAR detections to a facility scale to match AVIRIS-NG's resolution, reducing some biases. However, our theory suggests AVIRIS-NG plumes may still show higher emission rates due to small sources undetected by LIDAR, potentially overestimating the POD for AVIRIS-NG. They also combined ANG and GAO plume detections, which can introduce errors. Figure 4 shows that GAO's detection limit is superior to ANG's, likely due to GAO's smaller pixel size and the use of a visual camera.

The plume aggregation effect is relevant for comparing emission rates of trace gases like CO_2 and NO_2[78,79]. For instance, CO_2 plumes observed by coarse-resolution satellites (e.g., OCO-3) cover larger areas and show higher emission rates than those observed by fine-resolution satellites (e.g., PRISMA, EnMAP, EMIT) that observe plumes from specific sources like a power plant's smokestack[78,80].

7 Summary

We presented theoretical and empirical analyses to relate emission rate sums of sporadic plume detections with area estimates in dense point source emission fields. We used the Permian Basin's oil and gas sector emission data to show a strong linear relationship between plume sums and area estimates. This relationship enables the use of plume detections to evaluate and inform area estimates. After accounting for the plume detectors' sampling of the Permian emission field, we found that the weekly plume sums demonstrate a strong correlation with TROPOMI flux inversion area estimates. We demonstrated that the correlation remains robust, even with as few as 100 large plumes over a period of four to five weeks. This demonstration implies that informing area estimates should also be possible

using space-borne plume detectors, which have poorer detection sensitivity than aircraft instruments but have a significant advantage in spatial and temporal coverage. We presented a Bayesian framework to inform gridded area estimates using plume data. We improved the posterior's temporal variability by assimilating weekly plume sums on a temporally constant EDF inventory. By assimilating plume data, we corrected fine spatial resolution features of TROPOMI flux inversion emission estimates. In summary, our analysis showed that, with adequate sampling under favorable observation conditions, plume datasets can evaluate and inform area emission estimates of the oil and gas sector.

Plume detections are direct observations of emissions, enabling identification of the source location, sector, and time of large emissions. Area estimates constrain the total emissions, i.e., the area integral of the emission field. Both plume and area observation approaches provide unique and important information on emissions. Future research should test the applicability of the approach developed in this study on a broader spectrum of methane source sectors and possibly other trace gases (CO_2, CO, NO_2) observed at different spatial scales as plumes and area emission estimates.

Acknowledgement

Part of this work was carried out at the Jet Propulsion Laboratory, California Institute of Technology, under a contract with the National Aeronautics and Space Administration (80NM0018D0004). This research is supported by NASA ROSES Grant 18-CMS18-0018, 22-CMS22-0010, and the U.S. Greenhouse Gas Center.

Competing Interests: The authors declare that they have no conflict of interest.

A Appendix

A.1 Derivation of Statistical Relationship between Area Estimates and Plume Sums

We derive a statistical relation between the area estimates of grid cell emissions (representing mean emissions over a space and time interval) and the emission rate sum of plume detections from the grid cell. Consider a sector or sub-sector category (sector's component), s, composed of densely distributed point sources within a large grid cell c of area l_c^2 [distance^2]. The size of l_c^2 ranges from 25×25 km^2 (a regional flux inversion grid cell) to more than $5^\circ \times 5^\circ$ of latitude–longitude (a global flux inversion grid cell).

Suppose a plume instrument i with a spatial pixel size of l_i observes c. The instrument performs a number of scans covering different portions within the period of c. From these scans, plume detections are identified and quantified. Let η_{ic} [unitless] represent the instrument's *sampling* of c, which is the ratio of the total scanned ground area to the grid cell area l_c^2. For example, if an instrument scans half of a grid cell once, $\eta_{ic} = 0.5$, and if it scans the entire grid cell once, $\eta_{ic} = 1$. Assuming a uniform point source emission field, the number of plume detections in the second scenario would be twice that of the first scenario, shifting the entire frequency distribution up by a factor of two.

Suppose the emission spatial specificity of the instrument is δ_i, so that δ_i^2 is roughly the average of the plume area sizes that the instrument observes. Thus, the instrument effectively observes the emission field of c divided into $m = \left(\frac{l_c}{\delta_i}\right)^2$ small areas. Each δ_i^2-sized area will have an emission value e [mass time^{-1}].

Let $p_{ics}(e, \delta_i)$ [mass^{-1} time] represent the probability density function (PDF) of the emission values e [mass time^{-1}] for pixels of size δ_i^2 within grid cell c, for instrument i observing sector s, where $e > 0$. This PDF captures the full emission distribution of point sources in sector s within cell c at resolution δ_i. The total emission (or area estimate) in c,

denoted as x_{cs} [mass time^{-1}], is given by:

$$x_{cs} = \alpha_{cs} m \int_e p_{ics}(e, \delta_i) e de \tag{5}$$

Here, α_{cs} [unitless] is the emission activity factor in grid cell c. For example, α_{cs} could represent the number of gas wells in c when considering emissions from gas production. The term $\int_e p_{ics}(e, \delta_i) e de$ is the expected value of e corresponding to the PDF. As the emission rate distribution shifts to the right with increasing l_i (and δ_i) (see Figure 2), the expected value of the distribution shifts proportionally to δ_i^2. Therefore, the quantity $m \int_e p_{ics}(e, \delta_i) e de$ remains independent of δ_i, since $m = \left(\frac{l_c}{\delta_i}\right)^2$. This is necessary because the total area estimate x_{cs} should not depend on the plume-detecting instrument's properties.

Let $q_{ic}(e)$ denote the POD function of instrument i in the observation conditions of c. The frequency distribution ($f_{ics}(e)$) of observed plume emission rates can be modeled as:

$$f_{ics}(e) = \alpha_{cs} \eta_{ic} \kappa_{is} m \, p_{ics}(e, \delta_i) q_{ic}(e) \tag{6}$$

Here, κ_{is} [unitless] is a periodicity correction factor to account for the temporal sampling bias of instrument i observing plumes from sector s. κ_{is} is the ratio between total emissions at the observation time of the instrument and the temporal mean of the total emissions.

In a sector, emissions can be periodic, episodic, or continuous. An ergodic process is one in which the long-term time average of a single realization equals the overall expected value across all possible realizations. For plume distributions, this means that the time-averaged emissions from one location will match the expected emissions averaged across multiple locations. When the characteristic length l_c is sufficiently large to ensure representative sampling of independent and identically distributed (IID) episodic emitters, ergodicity allows the contribution from episodic emissions to be treated as constant over time. Consequently, only the periodicity of emissions introduces a temporal sampling bias.

Let y_{ics} [mass time^{-1}] denote the sum of emission rates of the observed plumes by i in

all the scans. Then,

$$y_{ics} = \alpha_{cs}\eta_{ic}\kappa_{is}m_{ic}\int_e p_{cs}(e,\delta_i)q_{ic}(e)ede \tag{7}$$

The relationship between the plume sum, y_{ics}, and the total area estimates x_{cs} can be derived using Equations 7 and 5:

$$y_{ics} = \tau_{ics}\kappa_{is}\eta_{ic}x_{cs} \tag{8}$$

Here, the unitless quantity

$$\tau_{ics} = \frac{\int_e p_{ics}(e,\delta_i)q_{ic}(e)ede}{\int_e p_{ics}(e,\delta_i)ede} \in [0,1] \tag{9}$$

represents the fraction of the total emissions of s that can be observed by instrument i. If $\eta_{ic} = 1$ (one complete scan of c by i) and there is no periodicity bias ($\kappa_{is} = 1$), then $\tau_{ics} = \frac{y_{ics}}{x_{cs}}$. We call τ the *plume factor*.

A.2 Bayesian Assimilation of Plume Observations

We can combine the information from plume detections and area estimates using Bayes' theorem. Let $\mathbf{x}$ be the vector of area estimates, where each element represents the total area emissions from a grid cell. Let $\mathbf{y}$ be the vector of plume sum observations, where each element represents the sum of emission rates of plume detections over the spatial and temporal intervals of the corresponding grid cell.

The conditional PDF $p(\mathbf{x}|\mathbf{y})$ of the area emission estimates vector $\mathbf{x}$ given the plume observation vector $\mathbf{y}$ is given by

$$p(\mathbf{x}|\mathbf{y}) = \frac{p(\mathbf{y}|\mathbf{x})p(\mathbf{x})}{p(\mathbf{y})} \tag{10}$$

Here, $p(\mathbf{y}|\mathbf{x})$ is the conditional PDF of the observed gridded plume sums given the area emission estimates. The functions $p(\mathbf{x})$ and $p(\mathbf{y})$ are the prior PDFs of $\mathbf{x}$ and $\mathbf{y}$, respectively.

$\mathbf{x}$ and $\mathbf{y}$ have the following relation:

$$\mathbf{y} = \mathbf{K}\mathbf{x} + \epsilon, \tag{11}$$

where $\mathbf{K} = \frac{\partial \mathbf{y}}{\partial \mathbf{x}}$ is a Jacobian matrix, whose entries can be estimated via the plume sum model (Equation 1). ϵ represents the combined errors in the observations and model. If the PDFs of $\mathbf{x}$ and $\mathbf{y}$ are assumed Gaussian, a quadratic cost function $J(\mathbf{x})$ can be derived as

$$-2\log p(\mathbf{y}|\mathbf{x}) \sim J(\mathbf{x}) = \underbrace{(\mathbf{x}-\mathbf{x_A})^T {\mathbf{S_A}}^{-1}(\mathbf{x}-\mathbf{x_A})}_{\text{Prior Constraint}} + \underbrace{(\mathbf{y}-\mathbf{K}\mathbf{x})^T {\mathbf{S}_\epsilon}^{-1}(\mathbf{y}-\mathbf{K}\mathbf{x})}_{\text{Observation Constraint}} \tag{12}$$

Here, $\mathbf{x_A}$ is a prior estimate of the area emissions vector, and $\mathbf{S_A}$ and $\mathbf{S}_\epsilon$ represent the prior and observational error covariance matrices of $\mathbf{x}$ and ϵ, respectively. The derivation of the cost function is provided in Lorenc[81], Brasseur and Jacob[82]. The cost function comprises two components: the error-weighted prior and error-weighted observational constraints. The minimization of the cost function yields the maximum a posteriori (MAP) solution, represented as the posterior area emissions estimate vector $\hat{\mathbf{x}}$:

$$\hat{\mathbf{x}} = \mathbf{x_A} + \hat{\mathbf{S}}\mathbf{K}^T {\mathbf{S}_\epsilon}^{-1}(\mathbf{y} - \mathbf{K}\mathbf{x_A}) \tag{13}$$

Here, $\hat{\mathbf{S}}$ denotes the posterior error covariance matrix, given by:

$$\hat{\mathbf{S}} = (\mathbf{K}^T {\mathbf{S}_\epsilon}^{-1}\mathbf{K} + {\mathbf{S_A}}^{-1})^{-1} \tag{14}$$

The averaging kernel matrix, $\mathbf{A}$, quantifies the sensitivity of the posterior solution to the truth. It can be calculated as follows:

$$\mathbf{A} = \mathbf{I} - \hat{\mathbf{S}}{\mathbf{S_A}}^{-1} \tag{15}$$

Here, $\mathbf{I}$ is an identity matrix. The trace of matrix $\mathbf{A}$ (the sum of its diagonal elements) is the *degrees of freedom for signal* (DOFS) of the inversion. The DOFS indicates the number of pieces of information constraining the state vector in the inversion.

We performed plume inversion on the Permian Basin oil and gas emissions using ANG and GAO plume observations from the Fall 2019 Carbon Mapper campaigns. The state vector $\mathbf{x}$ represents weekly area emission estimates (for a week period of Tuesday to Monday) over six weeks (September 24 to November 4, 2019) for each grid cell of 25×25 km^2 ($0.25^\circ \times 0.3125^\circ$). Two plume inversion analyses were conducted using different priors: (1) a constant bottom-up EDF inventory[68] (Plume-EDF inversion), and (2) the TROPOMI flux inversion from Varon et al.[9] (Plume-TRO inversion). TROPOMI flux inversion area estimates provide the total emissions from all sectors. Emissions from sectors other than oil and gas contribute only 6% to the Permian Basin's total emissions. In conducting the Plume-TRO inversion, these other emissions were estimated using the EDF inventory proportions and subtracted from the TROPOMI area emission estimates.

In the Plume-TRO inversion, $\mathbf{S_A}$ is the posterior error covariance matrix from Varon et al.[9]. For the Plume-EDF inversion, $\mathbf{S_A}$ is assumed to be a diagonal matrix with 100% standard deviation uncertainty.

The observation vector $\mathbf{y}$ is formed as:

$$\mathbf{y} = \begin{bmatrix} y_{i,1} & y_{i,2} & y_{i,3} & \cdots \end{bmatrix}^T, \text{ where } i \in \{\text{GAO}, \text{ANG}\} \tag{16}$$

Here, $y_{i,c}$ represents the sum of plume emission rates observed in the c-th grid cell (25×25 km^2) during a week period (Tuesday to Monday) by the instrument indexed by i. As per our model in Equation 1, the entries of the matrix $\mathbf{K}$ take the form:

$$k_{mn} = \begin{cases} \tau_{is}\kappa_{is}\eta_{ic} & \text{if } m = n = c \\ 0 & \text{otherwise} \end{cases} \tag{17}$$

where k_{mn} represents the element at the m-th row and n-th column of $\mathbf{K}$.

Table 1 presents the weekly $\tau_{is}\kappa_{is}$ and η_{ic} for the two instruments. For each instrument, we compute the mean of the weekly $\tau_{is}\kappa_{is}$ values. The uncertainty $\sigma_{\tau_{is}\kappa_{is}}$ is estimated as the 1 standard deviation ($\pm$) across the weekly values. We find $\tau_{is}\kappa_{is}$ values of 0.99 ± 0.06 for GAO and 0.75 ± 0.08 for ANG, respectively.

We modeled the observation error covariance matrix $\mathbf{S}_\epsilon$ as a diagonal matrix. All off-diagonal elements of $\mathbf{S}_\epsilon$ are set to zero. The diagonal elements at row and column m are calculated as the quadrature sum of plume observation error (σ_{y_m}), plume sum model error (σ_{k_m}), and sampling variance errors ($\sigma_{sampling_m}$).

$$\sigma^2_{\epsilon_m} = \sigma^2_{y_m} + \sigma^2_{sampling_m} + \sigma^2_{k_m} \tag{18}$$

where,

$$\sigma^2_{k_m} = \left(\frac{\sigma^2_{\tau_m \kappa_m}}{\tau^2_m \kappa^2_m} + \frac{\sigma^2_{\eta_m}}{\eta^2_m} \right) (\tau_m \kappa_m \eta_m x_{A_m})^2 \tag{19}$$

Here, x_{A_m} is the m^{th} element of $\mathbf{x_A}$. η_{ic} is calculated directly from the precise ground area of the flight tracks. The associated errors ($\sigma^2_{\eta_m}$) are negligible compared to other terms and are therefore disregarded in our plume inversions ($\sigma_{\eta_m} = 0$). $\sigma^2_{y_m}$ is calculated by adding the emission rate errors from the Carbon Mapper plume dataset in quadrature. $\sigma_{sampling_m}$ depends mainly on η_{ic}, decreasing with larger values of η_{ic}. We calculate it using the following relation:

$$\sigma_{sampling_m} = \frac{0.1}{\sqrt{\eta_m}} \tag{20}$$

This error model ensures that the sampling error diminishes with increased sampling, following the law of large numbers. A value of 0.1 t hr^{-1} is the assumed sampling error for one single complete scan of a grid cell.

B Data

B.1 Area Estimates of Emissions

EDF Bottom-up Inventory: We use the Environmental Defense Fund's (EDF) inventory presented in Zhang et al.[68]. This inventory estimates methane emissions by extrapolating ground-based measurements from several oil and gas production sites within the Permian Basin, focusing predominantly on the New Mexico area during July and August 2018. The sites were categorized based on their complexity into simple sites (equipped with wellheads and/or pump jacks) and complex sites (additionally featuring storage tanks and/or compressors). By extending these individual site emission rates to encompass the entire Permian Basin, the inventory estimates a basin-level methane emission rate of 2.3 Tg yr^{-1} from oil and gas production activities. The inventory also includes emissions from compressor stations and processing plants, estimated at 0.22 and 0.14 Tg yr^{-1}, respectively. The EDF inventory disaggregates these emissions to a $0.1^\circ \times 0.1^\circ$ grid, aligning with the spatial distribution of gas production. An updated version of the EDF inventory was published in Omara et al.[75]. We use the Zhang et al.[68] version in this study to maintain consistency with Varon et al.[9], who used this inventory as their Kalman Filter flux inversion prior.

TROPOMI Flux Inversion: We used the top-down methane emission data from the TROPOMI inversion analysis by Varon et al.[9]. They optimized emissions for the Permian Basin at resolutions of $0.25^\circ \times 0.3125^\circ$, equating to about 25 km $\times$ 25 km in the Permian Basin. The inversions used methane concentration observations from the TROPOspheric Monitoring Instrument (TROPOMI) on the Sentinel-5 Precursor satellite to estimate weekly methane emissions over the Permian Basin. TROPOMI, operational since May 2018, has a nadir-viewing push-broom configuration that captures methane concentration observations with a swath of 2600 km. The inversion used a nested version of the offline GEOS-Chem chemical transport model driven by NASA GEOS-FP meteorological fields. The model uses high-resolution grids and dynamic boundary conditions. The inversion used prior emission

estimates from the 2018 EDF inventory discussed above. The GEOS-Chem chemical transport model acted as a forward model, relating emissions to the TROPOMI observations in a Bayesian inverse modeling framework. This framework aimed to minimize discrepancies between model predictions and observations, constrained by prior emission estimates and error covariance matrices. The prior emissions were updated weekly, nudging closer to the original EDF bottom-up inventory values and setting initial conditions for subsequent analyses. For detailed information on these methodologies and the inversion results, we refer the reader to Varon et al.[9]. The mean emissions over 127 weeks (May 2018 to October 2020) were estimated at 4.05Tg yr^{-1}, 57% larger than the EDF 2018 inventory estimate of 2.58Tg yr^{-1}. Note that the weeks defined in Varon et al.[9] run from Tuesday to the following Monday, and we have used the same week period in our analysis.

B.2 Plume Observations

We use the plume detection data presented in Cusworth et al.[53]. The airborne survey, conducted by Carbon Mapper, aimed to quantify strong methane point sources in the Permian Basin. Between September and November 2019, Carbon Mapper deployed two remote sensing airborne platforms to map the region: the Next-Generation Airborne Visible/Infrared Imaging Spectrometer (AVIRIS-NG), henceforth referred to as ANG, and the Global Airborne Observatory (GAO). The GAO imaging spectrometer is identical to the ANG instrument; both were constructed by the NASA Jet Propulsion Laboratory around the same time. GAO is equipped with a Digital Modular Aerial Camera (DIMAC), bore-sighted with the imaging spectrometer, which provides simultaneous very high-resolution (VHR) visible imagery with approximately 60 cm ground pixel resolution during

The ANG instrument was flown at approximately 8 km altitude (above ground level) for 22 days between September 22nd and October 25th. It repeatedly surveyed subsections of the Delaware and Midland basins, areas with dense Oil and Gas activity (indicated by the darker red region in Figure 10). GAO, deployed at approximately 4.5 km altitude, surveyed

the extensive Permian (Delaware + Midland basins) over 21 flight days from October 10th to November 4th (black boxes in Figure 10A). The GAO flight boxes were designed to map the entire study domain once, capturing as much O&G infrastructure as possible, and overlapped with the AVIRIS-NG areas. The 4.5 km and 8 km flight altitudes of GAO and ANG allow for 4.5 m and 8 m ground pixel resolutions, respectively.

The two instruments measure ground-reflected backscattered solar radiance from 380 nm to 2510 nm at a 5 nm spectral resolution, allowing for methane slant column retrievals around the 2300 nm methane absorption feature. Flights were performed between 15:00 to 20:00 UTC (10:00-15:00 local time) to maximize solar light. The matched-filter method was employed to retrieve methane enhancement from the observed solar backscatter spectrum[3,83]. The observed spectrum is fitted to a background spectrum convolved with a target methane absorption spectrum, capturing the 2.3 μm absorption band. The method directly retrieves the methane enhancement above the background. All methane plumes from the instruments were determined visually using the retrieved methane maps. For classification as a plume, methane enhancements must have a spatial plume structure distinct from surface spectroscopy identifiable in the imaging spectrometer's RGB layers. The spatial extent of each plume was determined by extending radially outward from the origin of the plume and quantifying the maximum distance where significant methane was still detected above a 1000 ppm-m threshold. A maximum merge distance of 20 m was allowed between gaps in a plume, while a maximum distance threshold of 150 m was set for the plume's spatial extent. The plume locations are given in Figure 10. The plume emission rate was determined using the integrated Mass Enhancement Method (IME) from Duren et al.[31].

We excluded a few GAO flight lines from the analysis due to geolocation errors caused by poor orthorectification. These flight track lines, observed on 2019-10-13, 2019-10-16, and 2019-10-17, had lower plume counts than other tracks observing similar emissions activity areas. The excluded flight lines and corresponding plume detections are marked in gray in Figure 10.

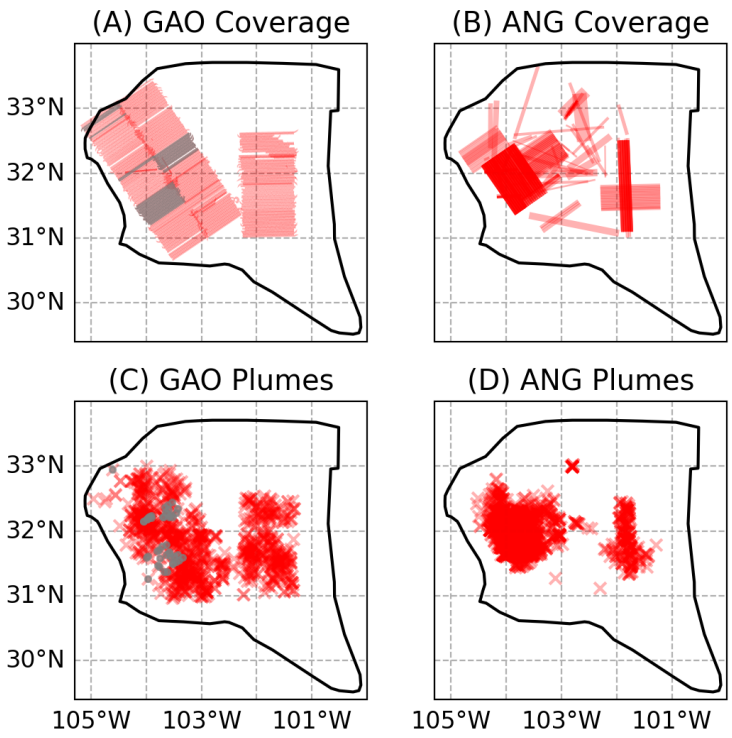

Figure 10: Spatial coverage and plume detection locations of ANG and GAO instruments for the Fall 2019 Carbon Mapper survey in the Permian Basin. The thick black contour marks the geological extent of the Permian Basin. Panels (A) and (B) show the coverage of GAO and ANG instruments, respectively, while Panels (C) and (D) display the plume detection locations for each instrument. The darker red regions indicate multiple overpasses in Panels (A) and (B). Poor performance of several GAO lines due to geolocation errors led to their exclusion from our analysis (marked in gray in the respective panels). The survey targeted two major hotspots of oil and gas activity in the Permian: the Delaware (West) and Midland (East) basins.

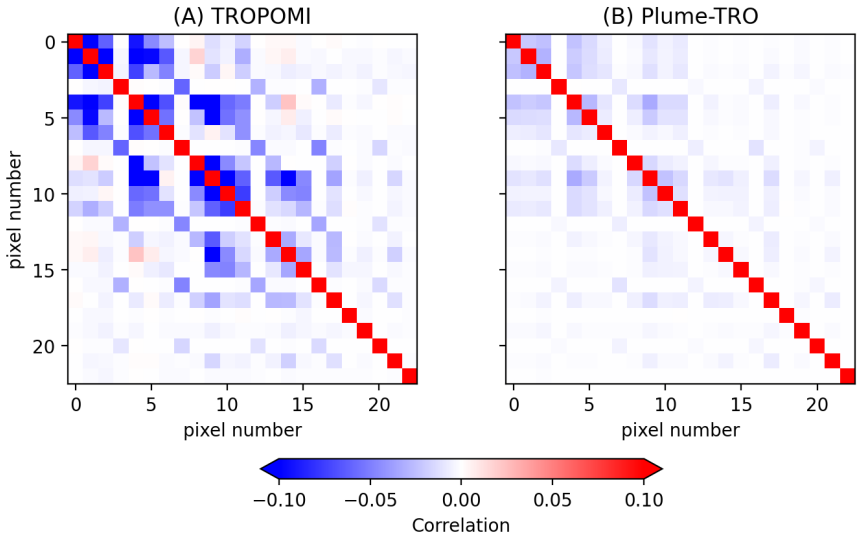

Figure 11: Improvement of the error correlation matrix by the Plume-TRO inversion for the week of Sep-27. Panel (A) shows the prior, and Panel (B) shows the posterior error correlation matrices of the Plume-TRO inversion. Only grid cells with plume detections during the week are shown.

References

(1) Brandt, A. R. et al. Methane leaks from North American natural gas systems. *Science (80-.).* **2014**, *343*, 733–735.

(2) Kort, E. A.; Frankenberg, C.; Costigan, K. R.; Lindenmaier, R.; Dubey, M. K.; Wunch, D. Four corners: The largest US methane anomaly viewed from space. *Geophys. Res. Lett.* **2014**, *41*, 6898–6903.

(3) Frankenberg, C.; Thorpe, A. K.; Thompson, D. R.; Hulley, G.; Kort, E. A.; Vance, N.; Borchardt, J.; Krings, T.; Gerilowski, K.; Sweeney, C.; Conley, S.; Bue, B. D.; Aubrey, A. D.; Hook, S.; Green, R. O. Airborne methane remote measurements reveal heavy-tail flux distribution in Four Corners region. *Proc. Natl. Acad. Sci.* **2016**, *113*, 9734–9739.

(4) Conley, S.; Franco, G.; Faloona, I.; Blake, D. R.; Peischl, J.; Ryerson, T. B. Methane

emissions from the 2015 Aliso Canyon blowout in Los Angeles, CA. *Science (80-.).* **2016**, *351*, 1317–1320.

(5) Zavala-Araiza, D.; Alvarez, R. A.; Lyon, D. R.; Allen, D. T.; Marchese, A. J.; Zimmerle, D. J.; Hamburg, S. P. Super-emitters in natural gas infrastructure are caused by abnormal process conditions. *Nat. Commun.* **2017**, *8*, 14012.

(6) Alvarez, R. A. et al. Assessment of methane emissions from the U.S. oil and gas supply chain. *Science (80-.).* **2018**, *361*, 186–188.

(7) Maasakkers, J. D.; Varon, D. J.; Elfarsdóttir, A.; McKeever, J.; Jervis, D.; Mahapatra, G.; Pandey, S.; Lorente, A.; Borsdorff, T.; Foorthuis, L. R.; Schuit, B. J.; Tol, P.; van Kempen, T. A.; van Hees, R.; Aben, I. Using satellites to uncover large methane emissions from landfills. *Sci. Adv.* **2022**, *8*, 1–9.

(8) Sherwin, E. D.; Rutherford, J. S.; Zhang, Z.; Chen, Y.; Wetherley, E. B.; Yakovlev, P. V.; Berman, E. S.; Jones, B. B.; Cusworth, D. H.; Thorpe, A. K.; Ayasse, A. K.; Duren, R. M.; Brandt, A. R. US oil and gas system emissions from nearly one million aerial site measurements. *Nature* **2024**, *627*, 328–334.

(9) Varon, D. J. et al. Continuous weekly monitoring of methane emissions from the Permian Basin by inversion of TROPOMI satellite observations. *Atmos. Chem. Phys.* **2023**, *23*, 7503–7520.

(10) Pandey, S.; Gautam, R.; Houweling, S.; Van Der Gon, H. D.; Sadavarte, P.; Borsdorff, T.; Hasekamp, O.; Landgraf, J.; Tol, P.; Van Kempen, T.; Hoogeveen, R.; Van Hees, R.; Hamburg, S. P.; Maasakkers, J. D.; Aben, I. Satellite observations reveal extreme methane leakage from a natural gas well blowout. *Proc. Natl. Acad. Sci. U. S. A.* **2019**, *116*, 26376–26381.

(11) Lauvaux, T.; Giron, C.; Mazzolini, M.; D'Aspremont, A.; Duren, R.; Cusworth, D.;

Shindell, D.; Ciais, P. Global assessment of oil and gas methane ultra-emitters. *Science (80-.).* **2022**, *375*, 557–561.

(12) Cusworth, D. H. et al. Quantifying methane emissions from United States landfills. *Science (80-.).* **2024**, *383*, 1499–1504.

(13) Nisbet, E. G. et al. Very Strong Atmospheric Methane Growth in the 4 Years 2014–2017: Implications for the Paris Agreement. *Global Biogeochem. Cycles* **2019**, *33*, 318–342.

(14) Ocko, I. B.; Sun, T.; Shindell, D.; Oppenheimer, M.; Hristov, A. N.; Pacala, S. W.; Mauzerall, D. L.; Xu, Y.; Hamburg, S. P. Acting rapidly to deploy readily available methane mitigation measures by sector can immediately slow global warming. *Environ. Res. Lett.* **2021**, *16*, 54042.

(15) UNEP International Methane Emissions Observatory. `https://www.unep.org/explore-topics/energy/what-we-do/methane/imeohttps://ec.europa.eu/commission/presscorner/detail/en/IP{\_}21{\_}5636`.

(16) Janssens-Maenhout, G. et al. EDGAR v4.3.2 Global Atlas of the three major greenhouse gas emissions for the period 1970-2012. *Earth Syst. Sci. Data* **2019**, *11*, 959–1002.

(17) Maasakkers, J. D.; Jacob, D. J.; Sulprizio, M. P.; Turner, A. J.; Weitz, M.; Wirth, T.; Hight, C.; DeFigueiredo, M.; Desai, M.; Schmeltz, R.; Hockstad, L.; Bloom, A. A.; Bowman, K. W.; Jeong, S.; Fischer, M. L. Gridded National Inventory of U.S. Methane Emissions. *Environ. Sci. Technol.* **2016**, *50*, 13123–13133.

(18) Houweling, S.; Kaminski, T.; Dentener, F.; Lelieveld, J.; Heimann, M. Inverse modeling of methane sources and sinks using the adjoint of a global transport model. *J. Geophys. Res.* **1999**, *104*, 26137–26160.

(19) Bergamaschi, P.; Frankenberg, C. Inverse modeling of global and regional CH$_4$ emissions using SCIAMACHY satellite retrievals. *J. Geophys. Res.* **2009**, *114*, 1–28.

(20) Monteil, G.; Houweling, S.; Butz, A.; Guerlet, S.; Schepers, D.; Hasekamp, O.; Frankenberg, C.; Scheepmaker, R.; Aben, I.; Röckmann, T. Comparison of CH$_4$ inversions based on 15 months of GOSAT and SCIAMACHY observations. *J. Geophys. Res. Atmos.* **2013**, *118*, 11,807–11,823.

(21) Miller, S. M.; Wofsy, S. C.; Michalak, A. M.; Kort, E. A.; Andrews, A. E.; Biraud, S. C.; Dlugokencky, E. J.; Eluszkiewicz, J.; Fischer, M. L.; Janssens-Maenhout, G.; Miller, B. R.; Miller, J. B.; Montzka, S. A.; Nehrkorn, T.; Sweeney, C. Anthropogenic emissions of methane in the United States. *Proc. Natl. Acad. Sci. U. S. A.* **2013**, *110*, 20018–20022.

(22) Pandey, S.; Houweling, S.; Krol, M.; Aben, I.; Chevallier, F.; Dlugokencky, E. J.; Gatti, L. V.; Gloor, E.; Miller, J. B.; Detmers, R.; Machida, T.; Röckmann, T. Inverse modeling of GOSAT-retrieved ratios of total column CH$_4$ and CO$_2$ for 2009 and 2010. *Atmos. Chem. Phys.* **2016**, *16*, 5043–5062.

(23) Zhang, Y.; J. Jacob, D.; Lu, X.; D. Maasakkers, J.; R. Scarpelli, T.; Sheng, J. X.; Shen, L.; Qu, Z.; P. Sulprizio, M.; Chang, J.; Anthony Bloom, A.; Ma, S.; Worden, J.; J. Parker, R.; Boesch, H. Attribution of the accelerating increase in atmospheric methane during 2010-2018 by inverse analysis of GOSAT observations. *Atmos. Chem. Phys.* **2021**, *21*, 3643–3666.

(24) Worden, J. R.; Cusworth, D. H.; Qu, Z.; Yin, Y.; Zhang, Y.; Bloom, A. A.; Ma, S.; Byrne, B. K.; Scarpelli, T.; Maasakkers, J. D.; Crisp, D.; Duren, R.; Jacob, D. J. The 2019 methane budget and uncertainties at 1° resolution and each country through Bayesian integration Of GOSAT total column methane data and a priori inventory estimates. *Atmos. Chem. Phys.* **2022**, *22*, 6811–6841.

(25) Basu, S.; Baker, D. F.; Chevallier, F.; Patra, P. K.; Liu, J.; Miller, J. B. The impact

of transport model differences on CO 2 surface flux estimates from OCO-2 retrievals of column average CO 2. **2018**, 7189–7215.

(26) Houweling, S.; Krol, M.; Bergamaschi, P.; Frankenberg, C.; Dlugokencky, E. J.; Morino, I.; Notholt, J.; Sherlock, V.; Wunch, D.; Beck, V.; Gerbig, C.; Chen, H.; Kort, E. A.; Röckmann, T.; Aben, I. A multi-year methane inversion using SCIAMACHY, accounting for systematic errors using TCCON measurements. *Atmos. Chem. Phys.* **2014**, *14*, 3991–4012.

(27) Schuh, A. E.; Byrne, B.; Jacobson, A. R.; Crowell, S. M.; Deng, F.; Baker, D. F.; Johnson, M. S.; Philip, S.; Weir, B. On the role of atmospheric model transport uncertainty in estimating the Chinese land carbon sink. *Nature* **2022**, *603*, E13–E14.

(28) Balasus, N.; Jacob, D. J.; Lorente, A.; Maasakkers, J. D.; Parker, R. J.; Boesch, H.; Chen, Z.; Kelp, M. M.; Nesser, H.; Varon, D. J. A blended TROPOMI+GOSAT satellite data product for atmospheric methane using machine learning to correct retrieval biases. *Atmos. Meas. Tech.* **2023**, *16*, 3787–3807.

(29) Kunkel, W. M.; Carre-Burritt, A. E.; Aivazian, G. S.; Snow, N. C.; Harris, J. T.; Mueller, T. S.; Roos, P. A.; Thorpe, M. J. Extension of Methane Emission Rate Distribution for Permian Basin Oil and Gas Production Infrastructure by Aerial LiDAR. *Environ. Sci. Technol.* **2023**, *57*, 12234–12241.

(30) Jervis, D.; McKeever, J.; Durak, B. O.; Sloan, J. J.; Gains, D.; Varon, D. J.; Ramier, A.; Strupler, M.; Tarrant, E. The GHGSat-D imaging spectrometer. *Atmos. Meas. Tech.* **2021**, *14*, 2127–2140.

(31) Duren, R. M. et al. California ' s methane super-emitters. *Nature* **2019**, *575*, 180–184.

(32) Guanter, L.; Irakulis-Loitxate, I.; Gorroño, J.; Sánchez-García, E.; Cusworth, D. H.; Varon, D. J.; Cogliati, S.; Colombo, R. Mapping methane point emissions with the PRISMA spaceborne imaging spectrometer. *Remote Sens. Environ.* **2021**, *265*, 112671.

(33) Varon, D. J.; Jervis, D.; McKeever, J.; Spence, I.; Gains, D.; Jacob, D. J. High-frequency monitoring of anomalous methane point sources with multispectral Sentinel-2 satellite observations. *Atmos. Meas. Tech.* **2021**, *14*, 2771–2785.

(34) Cusworth, D. H.; Thorpe, A. K.; Ayasse, A. K.; Stepp, D.; Heckler, J.; Asner, G. P.; Miller, C. E.; Yadav, V.; Chapman, J. W.; Eastwood, M. L.; Green, R. O.; Hmiel, B.; Lyon, D. R.; Duren, R. M. Strong methane point sources contribute a disproportionate fraction of total emissions across multiple basins in the United States. *Proc. Natl. Acad. Sci. U. S. A.* **2022**, *119*, 1–7.

(35) Chen, Y.; Sherwin, E. D.; Berman, E. S.; Jones, B. B.; Gordon, M. P.; Wetherley, E. B.; Kort, E. A.; Brandt, A. R. Quantifying Regional Methane Emissions in the New Mexico Permian Basin with a Comprehensive Aerial Survey. *Environ. Sci. Technol.* **2022**, *56*, 4317–4323.

(36) Johnson, M. R.; Conrad, B. M.; Tyner, D. R. Creating measurement-based oil and gas sector methane inventories using source-resolved aerial surveys. *Commun. Earth Environ.* **2023**, *4*, 1–9.

(37) Rutherford, J. S.; Sherwin, E. D.; Ravikumar, A. P.; Heath, G. A.; Englander, J.; Cooley, D.; Lyon, D.; Omara, M.; Langfitt, Q.; Brandt, A. R. Closing the methane gap in US oil and natural gas production emissions inventories. *Nat. Commun.* **2021**, *12*, 1–12.

(38) Lyon, D. R.; Zavala-Araiza, D.; Alvarez, R. A.; Harriss, R.; Palacios, V.; Lan, X.; Talbot, R.; Lavoie, T.; Shepson, P.; Yacovitch, T. I.; Herndon, S. C.; Marchese, A. J.; Zimmerle, D.; Robinson, A. L.; Hamburg, S. P. Constructing a Spatially Resolved Methane Emission Inventory for the Barnett Shale Region. *Environ. Sci. Technol.* **2015**, *49*, 8147–8157.

(39) Naus, S.; Maasakkers, J. D.; Gautam, R.; Omara, M.; Stikker, R.; Veenstra, A. K.;

Nathan, B.; Irakulis-Loitxate, I.; Guanter, L.; Pandey, S.; Girard, M.; Lorente, A.; Borsdorff, T.; Aben, I. Assessing the Relative Importance of Satellite-Detected Methane Superemitters in Quantifying Total Emissions for Oil and Gas Production Areas in Algeria. *Environ. Sci. Technol.* **2023**, *57*, 19545–19556.

(40) Xia, H.; Strayer, A.; Ravikumar, A. P. The role of emission size distribution on the efficacy of new technologies to reduce methane emissions from the oil and gas sector. *Environ. Sci. Technol.* **2024**, *58*, 1088–1096.

(41) Zimmerle, D.; Vaughn, T.; Bell, C.; Bennett, K.; Deshmukh, P.; Thoma, E. Detection Limits of Optical Gas Imaging for Natural Gas Leak Detection in Realistic Controlled Conditions. *Environ. Sci. Technol.* **2020**, *54*, 11506–11514.

(42) Omara, M.; Zimmerman, N.; Sullivan, M. R.; Li, X.; Ellis, A.; Cesa, R.; Subramanian, R.; Presto, A. A.; Robinson, A. L. Methane emissions from natural gas production sites in the United States: Data synthesis and national estimate. *Environ. Sci. Technol.* **2018**, acs.est.8b03535.

(43) Berman, E. S. F.; Wetherley, E. B.; Jones, B. B. Kairos Aerospace: Technical White Paper: Methane Detection.

(44) Irakulis-loitxate, A. I.; Guanter, L.; Maasakkers, J. D.; Zavala, D. Satellites unveil easily-fixable super-emissions in one of the world ' s largest methane hotspot regions. 1–32.

(45) Sánchez-García, E.; Gorroño, J.; Irakulis-Loitxate, I.; Varon, D. J.; Guanter, L. Mapping methane plumes at very high spatial resolution with the WorldView-3 satellite. *Atmos. Meas. Tech.* **2022**, *15*, 1657–1674.

(46) Cusworth, D. H. et al. Multisatellite Imaging of a Gas Well Blowout Enables Quantification of Total Methane Emissions. *Geophys. Res. Lett.* **2021**, *48*, 1–9.

(47) Pandey, S.; Houweling, S.; Krol, M.; Aben, I. Influence of Atmospheric Transport on Estimates of Variability in the Global Methane Burden Geophysical Research Letters. *Geophys. Res. Lett.* **2019**, *46*, 2302–2311.

(48) Varon, D. J.; McKeever, J.; Jervis, D.; Maasakkers, J. D.; Pandey, S.; Houweling, S.; Aben, I.; Scarpelli, T.; Jacob, D. J. Satellite Discovery of Anomalously Large Methane Point Sources From Oil/Gas Production. *Geophys. Res. Lett.* **2019**, *46*, 13507–13516.

(49) Maasakkers, J. D.; Omara, M.; Gautam, R.; Lorente, A.; Pandey, S.; Tol, P.; Borsdorff, T.; Houweling, S.; Aben, I. Reconstructing and quantifying methane emissions from the full duration of a 38-day natural gas well blowout using space-based observations. *Remote Sens. Environ.* **2022**, *270*, 112755.

(50) Pandey, S.; van Nistelrooij, M.; Maasakkers, J. D.; Sutar, P.; Houweling, S.; Varon, D. J.; Tol, P.; Gains, D.; Worden, J.; Aben, I. Daily detection and quantification of methane leaks using Sentinel-3: a tiered satellite observation approach with Sentinel-2 and Sentinel-5p. *Remote Sens. Environ.* **2023**, *296*, 113716.

(51) Ehret, T.; De Truchis, A.; Mazzolini, M.; Morel, J. M.; D'Aspremont, A.; Lauvaux, T.; Duren, R.; Cusworth, D.; Facciolo, G. Global Tracking and Quantification of Oil and Gas Methane Emissions from Recurrent Sentinel-2 Imagery. *Environ. Sci. Technol.* **2022**, *56*, 10517–10529.

(52) Jacob, D. J.; Varon, D. J.; Cusworth, D. H.; Dennison, P. E.; Frankenberg, C.; Gautam, R.; Guanter, L.; Kelley, J.; Mckeever, J.; Ott, L. E.; Poulter, B.; Qu, Z.; Thorpe, A. K.; Worden, J. R.; Duren, R. M. Quantifying methane emissions from the global scale down to point sources using satellite observations of atmospheric methane. *Atmos. Chem. Phys.* **2022**, 9617–9646.

(53) Cusworth, D. H.; Duren, R. M.; Thorpe, A. K.; Olson-Duvall, W.; Heckler, J.; Chapman, J. W.; Eastwood, M. L.; Helmlinger, M. C.; Green, R. O.; Asner, G. P.; Den-

nison, P. E.; Miller, C. E. Intermittency of Large Methane Emitters in the Permian Basin. *Environ. Sci. Technol. Lett.* **2021**, *8*, 567–573.

(54) Schuit, B. J. et al. Automated detection and monitoring of methane super-emitters using satellite data. *Atmos. Chem. Phys.* **2023**, *23*, 9071–9098.

(55) Thorpe, A. K. et al. Mapping methane concentrations from a controlled release experiment using the next generation airborne visible/infrared imaging spectrometer (AVIRIS-NG). *Remote Sens. Environ.* **2016**, *179*, 104–115.

(56) Conrad, B. M.; Tyner, D. R.; Johnson, M. R. Robust probabilities of detection and quantification uncertainty for aerial methane detection: Examples for three airborne technologies. *Remote Sens. Environ.* **2023**, *288*, 113499.

(57) Vaughn, T. L.; Bell, C. S.; Pickering, C. K.; Schwietzke, S.; Heath, G. A.; Pétron, G.; Zimmerle, D. J.; Schnell, R. C.; Nummedal, D. Temporal variability largely explains top-down/bottom-up difference in methane emission estimates from a natural gas production region. *Proc. Natl. Acad. Sci. U. S. A.* **2018**, *115*, 11712–11717.

(58) Allen, D. T.; Cardoso-Saldaña, F. J.; Kimura, Y. Variability in Spatially and Temporally Resolved Emissions and Hydrocarbon Source Fingerprints for Oil and Gas Sources in Shale Gas Production Regions. *Environ. Sci. Technol.* **2017**, *51*, 12016–12026.

(59) Sherwin, E. D.; Rutherford, J. S.; Chen, Y.; Aminfard, S.; Kort, E. A.; Jackson, R. B.; Brandt, A. R. Single-blind validation of space-based point-source detection and quantification of onshore methane emissions. *Sci. Rep.* **2023**, *13*, 1–10.

(60) Nesser, H.; Jacob, D. J.; Maasakkers, J. D.; Lorente, A.; Chen, Z.; Lu, X.; Shen, L.; Qu, Z.; Sulprizio, M. P.; Winter, M.; Ma, S.; Bloom, A. A.; Worden, J. R.; Stavins, R. N.; Randles, C. A. High-resolution US methane emissions inferred from an inversion of 2019 TROPOMI satellite data: contributions from individual states, urban areas, and landfills. *Atmos. Chem. Phys.* **2024**, *24*, 5069–5091.

(61) Turner, A. J. et al. Estimating global and North American methane emissions with high spatial resolution using GOSAT satellite data. *Atmos. Chem. Phys.* **2015**, *15*, 7049–7069.

(62) Meirink, J. F.; Bergamaschi, P.; Krol, M. C. Four-dimensional variational data assimilation for inverse modelling of atmospheric methane emissions: method and comparison with synthesis inversion. *Atmos. Chem. Phys.* **2008**, *8*, 6341–6353.

(63) Maasakkers, J. D.; McDuffie, E. E.; Sulprizio, M. P.; Chen, C.; Schultz, M.; Brunelle, L.; Thrush, R.; Steller, J.; Sherry, C.; Jacob, D. J.; Jeong, S.; Irving, B.; Weitz, M. A Gridded Inventory of Annual 2012-2018 U.S. Anthropogenic Methane Emissions. *Environ. Sci. Technol.* **2023**, *57*, 16276–16288.

(64) Jacob, D. J.; Turner, A. J.; Maasakkers, J. D.; Sheng, J.; Sun, K.; Liu, X.; Chance, K.; Aben, I.; McKeever, J.; Frankenberg, C. Satellite observations of atmospheric methane and their value for quantifying methane emissions. *Atmos. Chem. Phys.* **2016**, *16*, 14371–14396.

(65) Buchwitz, M.; Schneising, O.; Reuter, M.; Heymann, J.; Krautwurst, S.; Bovensmann, H.; Burrows, J. P.; Boesch, H.; Parker, R. J.; Detmers, R. G.; Hasekamp, O. P.; Aben, I.; Butz, A.; Frankenberg, C. Satellite-derived methane hotspot emission estimates using a fast data-driven method. *Atmos. Chem. Phys.* **2017**, 5751–5774.

(66) Pandey, S.; Houweling, S.; Lorente, A.; Borsdorff, T.; Tsivlidou, M.; Anthony Bloom, A.; Poulter, B.; Zhang, Z.; Aben, I. Using satellite data to identify the methane emission controls of South Sudan's wetlands. *Biogeosciences* **2021**, *18*, 557–572.

(67) Feldman, A. F.; Zhang, Z.; Yoshida, Y.; Chatterjee, A.; Poulter, B. Using Orbiting Carbon Observatory-2 (OCO-2) column CO$_{2}$ retrievals to rapidly detect and estimate biospheric surface carbon flux anomalies. *Atmos. Chem. Phys.* **2023**, *23*, 1545–1563.

(68) Zhang, Y. et al. Quantifying methane emissions from the largest oil-producing basin in the United States from space. *Sci. Adv.* **2020**, *6*, 1–10.

(69) Irakulis-Loitxate, I.; Guanter, L.; Maasakkers, J. D.; Zavala-Araiza, D.; Aben, I. Satellites Detect Abatable Super-Emissions in One of the World's Largest Methane Hotspot Regions. *Environ. Sci. Technol.* **2022**, *56*, 2143–2152.

(70) Rouet-Leduc, B.; Hulbert, C. Automatic detection of methane emissions in multispectral satellite imagery using a vision transformer. *Nat. Commun.* **2024**, *15*, 1–9.

(71) Lauvaux, T.; Giron, C.; Mazzolini, M.; D'Aspremont, A.; Duren, R.; Cusworth, D.; Shindell, D.; Ciais, P. Global assessment of oil and gas methane ultra-emitters. *Science (80-.).* **2022**, *375*, 557–561.

(72) United Nations Environment Programme (UNEP) Methane Alert and Response System (MARS). \url{https://methanedata.unep.org/plumemap?mars=false}, 2023; `https://methanedata.unep.org/plumemap?mars=false`.

(73) Zavala-Araiza, D. et al. Reconciling divergent estimates of oil and gas methane emissions. *Proc. Natl. Acad. Sci. U. S. A.* **2015**, *112*, 15597–15602.

(74) Allen, D. T.; Torres, V. M.; Thomas, J.; Sullivan, D. W.; Harrison, M.; Hendler, A.; Herndon, S. C.; Kolb, C. E.; Fraser, M. P.; Hill, A. D.; Lamb, B. K.; Miskimins, J.; Sawyer, R. F.; Seinfeldi, J. H. Measurements of methane emissions at natural gas production sites in the United States. *Proc. Natl. Acad. Sci. U. S. A.* **2013**, *110*, 17768–17773.

(75) Omara, M.; Himmelberger, A.; Mackay, K.; Williams, J. P.; Benmergui, J.; Sargent, M.; Wofsy, S. C.; Gautam, R. Constructing a measurement-based spatially explicit inventory of US oil and gas methane emissions. **2024**, 1–25.

(76) Hamburg, S.; Gautam, R.; Zavala-Araiza, D. MethaneSAT - A New Tool Purpose-Built to Measure Oil and Gas Methane Emissions from Space. 2022; https://doi.org/10.2118/210922-MS.

(77) NASA New Proposals to Help NASA Advance Knowledge of Our Changing Climate. \url{https://www.nasa.gov/news-release/new-proposals-to-help-nasa-advance-knowledge-of-our-changing-climate/}, 2024.

(78) Cusworth, D. H.; Thorpe, A. K.; Miller, C. E.; Ayasse, A. K.; Jiorle, R.; Duren, R. M.; Nassar, R.; Mastrogiacomo, J. P.; Nelson, R. R. Two years of satellite-based carbon dioxide emission quantification at the world's largest coal-fired power plants. *Atmos. Chem. Phys.* **2023**, *23*, 14577–14591.

(79) Varon, D. J.; Jervis, D.; Pandey, S.; Gallardo, S. L.; Balasus, N.; Yang, L. H.; Jacob, D. J. Quantifying NOx point sources with Landsat and Sentinel-2 satellite observations of NO2 plumes. *Proc. Natl. Acad. Sci.* **2024**, *121*, e2317077121.

(80) Thorpe, A. K. et al. Attribution of individual methane and carbon dioxide emission sources using EMIT observations from space. *Sci. Adv.* **2023**, *9*, eadh2391.

(81) Lorenc, A. C. Analysis methods for numerical weather prediction. *Q. J. R. Meteorol. Soc.* **1986**, *112*, 1177–1194.

(82) Brasseur, G. P.; Jacob, D. J. *Model. Atmos. Chem.*; Cambridge University Press, 2017; pp 487–537.

(83) Thompson, D. R.; Thorpe, A. K.; Frankenberg, C.; Green, R. O.; Duren, R.; Guanter, L.; Hollstein, A.; Middleton, E.; Ong, L.; Ungar, S. Space-based remote imaging spectroscopy of the Aliso Canyon CH4 superemitter. *Geophys. Res. Lett.* **2016**, *43*, 6571–6578.